University of Alberta

Analysis of Ultra-Wideband Pulse Scattered from Planar Objects

by

Lin Li

A thesis submitted to the Faculty of Graduate Studies and Research
in partial fulfillment of the requirements for the degree of

Master of Science

in

Electromagnetics and Microwave

Department of Electrical and Computer Engineering

Spring 2012
Edmonton, Alberta

Dedication

To my Parents

Abstract

Ultra-wideband (UWB) pulses scattered from objects contain essential information. By analyzing the scattered pulse, the objects can be located, imaged and characterized. This thesis focuses on characterizing physical and electrical properties of planar metallic and dielectric objects by analyzing the scattered UWB pulse.

In the analysis of UWB pulse scattered from planar metallic objects, we establish an analytical model to estimate the scattered UWB pulse. Furthermore, we formulate a frequency-averaged radar cross section (RCS) to estimate the radar signature of an object based on UWB radar measurements. In the analysis of UWB pulse scattered from planar dielectric objects buried in ground, we establish a numerical model, based on mean square error (MSE) method, to estimate the depth, thickness and complex permittivity of the buried objects.

Multiple experiments validate the proposed methodologies of analyzing the scattered UWB pulse from the planar objects, providing agreement between the measured results and proposed theory.

Acknowledgements

It is my pleasure to be a member of Dr. Rambabu Karumudi's research group. I would like to take this opportunity to show my gratitude to my fellow labmates. This thesis would not have been possible without their support.

I would like to express my heartfelt gratitude to my supervisor, Dr. Rambabu Karumudi for his tireless dedication and constant encouragement in helping me to achieve my career objectives. He is always the source of inspiration for me when I encountered technical difficulties. I firmly believe I have benefited enormously from my experience of working with him, not only in completing the research, but also in personal development.

My special thanks go to Dr. Adrian Eng-Choon Tan for sharing his rich experience in ultra-wideband radars. His technical suggestions helped in increasing the accuracy of the modeling in this research. Additionally, his academic writing skills helped me improve my technical writing. I am also deeply grateful to Mr. Kevin Khee-Meng Chan for his patience and caring attitude both technically and personally. His extensive industrial experience always guided me in effectively conducting my experiments. I sincerely acknowledge Mr. Kashish Jhamb for his discussion and assistance in verifications of the proposed methodologies both in simulation and experiments.

Last but not least. I wish to express my gratitude to my mom and dad for their spiritual encouragement and endless love, especially during my time away from home.

Table of Contents

List of Tables

List of Figures

List of Symbols

d	Distance / thickness / depth
$\mathcal{E}$	Energy
E	Electric field
$\mathcal{F}$	Fidelity factor
G	Antenna gain
$h_r(t)$	Antenna transfer function in receiving mode
$h_t(t)$	Antenna transfer function in transmitting mode
$H(\omega)$	System transfer function of boresight antenna system
$H_R(\omega)$	Antenna transfer function in receiving mode in frequency domain
$H_T(\omega)$	Antenna transfer function in transmitting mode in frequency domain
le	Antenna effective height
lp	Antenna physical height
$m(t)$	Target response
$M(\omega)$	Target response in frequency domain
P	Power
$p(t)$	Path loss factor
$r(t)$	Received pulse
$R(\omega)$	Received pulse in frequency domain
$s(t)$	Excitation pulse
$S(\omega)$	Excitation pulse in frequency domain
U	Energy density
$v(t)$	Received signal
W	Power density
$y(t)$	Object transfer function
Z_0	Characteristic impedance
Z	Input impedance

Γ	Reflection coefficient
γ	Propagation constant
ε_r	Relative dielectric permittivity
η_0	Intrinsic impedance of free-space
θ_i	Incident angle
θ_t	Refracted angle
σ_{avg}	Frequency-averaged radar cross section

List of Abbreviations

ADC	Analog-to-digital converter
DDS	Direct digital synthesizer
EIRP	Equivalent isotropically radiated power
EM	Electromagnetic
FDTD	Finite difference time domain
FEM-BEM	Finite- and boundary- element method
GPR	Ground penetrating radar
IFN	Impulse forming network
LNA	Low noise amplifier
MSE	Mean square error
MUT	Material under test
PA	Power amplifier
PEC	Perfect electrical conductor
PRF	Pulse repetition frequency
RCS	Radar cross section
RHP	Riemann-Hilbert method
Rx	Receiving
SCM	Single chip microcomputer

SNR	Signal-to-noise ratio
SRD	Step recovery diode
TBM	Tunnel boring machine
TOA	Time-of-arrival
Tx	Transmitting
UWB	Ultra-wideband
3D	Three-dimensional

Chapter-I

1 Introduction

1.1 Background

Ultra-wideband (UWB) radio is a low-power, short-range, high-bandwidth wireless communication technology that transmits and receives signals via the exchange of electromagnetic (EM) pulses [1]. The short pulse width property of UWB signals enhances their direct resolvability of discrete multipath components [2] and provides diversity gain by combining multipath components [3]. In addition, the carrierless transmission property of UWB pulses simplifies and miniaturizes their transceiver designs [4]. A radiated UWB pulse gets scattered when it impinges on electromagnetically opaque objects. The study of scattered UWB pulses is of significant importance for various applications. In antenna designs, researchers have optimized antenna radiation patterns by reducing the strut blockage or coating antennas with soft and hard surfaces [5-7]. In medical and hygiene fields, scientists have diagnosed breast cancer based on the difference in the scattered UWB pulses from normal and tumor breast tissues [8-10]. The scattering of UWB pulses is also employed in the construction industry to monitor concrete structure health [11, 12]. UWB radars are extensively employed to detect and localize moving targets [13] and measure radar cross section (RCS) [14]. Based on RCS measurements, scientists have estimated the speed and direction of the wind, and the surface temperature of the ocean [15-17]. Additionally, the RCS is an important signature in detecting, tracking and identifying aircrafts, ships and missiles as well as developing counter measures such as RCS reduction and stealth design [18-20].

UWB technology is also extensively used in ground penetrating radar (GPR) [21]. UWB GPR is a short-range radar system that remotely senses and images objects that are buried beneath the ground. It radiates a sequence of short electromagnetic pulses into the ground while simultaneously measuring reflections due to discontinuities in the electrical properties of the multilayer structure of the ground.

UWB GPRs have been found to be extremely useful in probing subsurface targets. Their ability to map buried objects and interfaces has been documented in numerous ground-probing applications since the early 1970s. UWB GPR technology is also applied in detecting and locating potential buried hazards such as mine shafts and voids in the mining industry [22], studying the structure and formation of glaciers [23], uncovering forensic evidence including buried human remains and weapons [24], investigating archaeological sites [25], and detecting and characterizing unexploded ordnance [26]. In the construction industry, UWB GPRs have been used in locating buried pipes and utility installations [27], investigating concrete structures to determine reinforcing bar locations, air voids, and the quality of concrete [28], and checking the integrity of road and pavement sub-surfaces [29].

1.2 Literature Review

In the literature, techniques for computing scattered electromagnetic waves due to various objects have been extensively studied. Finite difference time domain (FDTD) method was used to find the near scattered fields and then compute the far scattered fields [30]. Unimoment method and patch imitation method for induced electric current were combined to calculate both the electric and magnetic fields

scattered by an irregular metal surface [31]. The finite- and boundary-element method (FEM-BEM) was employed to extract the frequency dependent scattering parameters of a short metal reflector [32]. The transmission-line and diffraction theories were used to estimate the electromagnetic field scattered by metal wires and metal sheets [33].

In terms of the RCS, Herberthson proposed the potential method to estimate the RCS of electrically large objects [34]. Geometric diffraction theory was applied to estimate the scattered fields and RCS of right circular cones [35]. Quasi-static approximation and graphical electromagnetic computing were used to predict the RCS of in-flight aircraft [36]. A dual-series-based Riemann-Hilbert method (RHP) was used to study the RCS of cylindrical cavity-backed apertures[37].

In the mean-time, several methods of measuring the electrical properties of materials have been reported. These methods can be classified into transmission [38] and reflection [39] methods, the two-terminal method [40], the loaded transmission line method [41], the closed cavity method [42], the open resonator method [43], the microwave free-space method [44] and the stochastic cavity method [45]. A review of these methods can be found in [46]. Electrical properties of the object can be estimated by post-processing the received reflected signals and solving an inverse electromagnetic problem using different techniques [47]. However, due to the ill-posed nature of this inverse problem, the solution is inherently non-unique by virtue of the equivalence principle [48]. The most widely used method is the inverse scattering method, in which optimization is performed to determine the object parameters such as dielectric properties and dimensions [49]. Another popular method of determining the dielectric properties is the layer

stripping method [29], in which reflections from different layers of the object are estimated, and subtracted from the received signal until all the reflections have been accounted for. In recent years, electromagnetic simulation software, such as Ansys HFSS and CST Microwave Studio, have been employed to estimate the dielectric properties of arbitrarily shaped objects [50]. Optimization techniques are also being used extensively to solve the inverse problems. The concerns with these techniques are their speed, resource requirement and convergence. To address the inverse problem, various numerical techniques have been proposed including the Newton-Raphson method [51], gradient descent optimization [50], genetic algorithm [52] and different variants of the sequential quadratic programming method [42, 53].

1.3 Contributions

Although the scattered electromagnetic fields and the RCS of objects were extensively investigated in [30-37, 54-58], the relationship between the scattered electromagnetic field and characteristics of the scattered pulse has not been established. This thesis proposes a method of characterizing both the amplitude and shape of the UWB pulse scattered from metal planar objects in far-field. When the object is in the near-field, the transition of the scattered pulse shape is studied. The proposed method is also used to study the effect of multiple scattering on the shape and amplitude of the scattered pulse. In addition, we derived a closed-form frequency-averaged RCS of the metal planar object.

To characterize the buried object in the ground, our proposed method differs from the existing literature in three ways. First, the estimated real and imaginary permittivity profiles of the buried object are frequency dependent. Second, we have

improved the parameter optimization process by enforcing a constant object depth and thickness at all frequencies. Third, path loss due to the close proximity of the UWB GPR to the ground has been compensated analytically.

1.4 Organization of the thesis

Chapter 2 analyzes both the amplitude and shape of the UWB pulse scattered from metal planar objects. We also define a frequency-averaged RCS of the metal planar object that helps estimate the coverage area of the radar. Chapter 3 presents a method of estimating the thickness, depth and complex permittivity of the buried object by using UWB GPR. Chapter 4 concludes the work presented in this thesis and discusses future research directions for the analysis of the scattered UWB pulse from electromagnetically opaque objects.

Chapter-II

2 Characteristics of Ultra-Wideband Pulse Scattered from Planar Objects

Introduction

In this chapter, a method of estimating the characteristics of ultra-wideband (UWB) pulse scattered from metal planar objects in far-field [48] is proposed. When the object is in near-field [48], the transition of the scattered pulse shape is studied. In addition, we define a frequency-averaged radar cross section (RCS) of the metal planar object in terms of the effective height of the transmitting and receiving antennas, and the energy of the excitation and received pulses. We find excellent agreement between the estimated and measured scattered pulses for metal planar objects of sizes 100 X 100 mm^2, 160 X 160 mm^2 and 200 X 200 mm^2. For the same objects, the estimated frequency-averaged RCS are close to narrowband conventional RCS. The agreement validates the proposed method, allowing us to compute the scattered pulse shape and energy based on the conventional RCS [59] of the object.

This chapter is organized as follows: In section 2.1, a method of estimating the amplitude and shape of the scattered pulse from a metal planar object is presented. Section 2.2 studies the transition of pulse shape as a function of distance from the scattering object. Section 2.3 studies the effect of multiple scatterers on the pulse shape. In section 2.4, a frequency-averaged RCS of a metal planar object is derived.

2.1 Modeling the UWB Pulse Scattered from a Metal Planar Object

2.1.1 Overview

In this section, we propose a method of predicting both the amplitude and shape of the scattered pulse from a metal planar object. As shown in Fig. 2.1 the transmitting (Tx) and receiving (Rx) ultra-wideband (UWB) antennas are placed in a monostatic radar configuration. The distance between the radar and the object (R) ensures far-field conditions. The Tx antenna is excited with a sub-nanosecond pulse, $s(t)$. The radiated pulse is scattered by the metal planar object and is received by the Rx antenna as $r_m(t)$. $E^i(\omega,R)$ is the incident electric field of the pulse on the metal planar object; $E^s(\omega)$ is the scattered electric field on the aperture of the Rx antenna; $P^r(\omega,R)$ is the scattered power at the object surface; $m(t)$ is the target response of the metal planar object that relates the scattered power ($P^r(\omega,R)$) and the incident electric field ($E^i(\omega,R)$); $h_t(t)$ and $h_r(t)$ are the transfer function of the antennas in Tx and Rx modes; ω is the angular frequency. The analysis begins with the derivation of the target response of the metal planar object, and then the transfer function of the UWB antennas in Tx and Rx modes.

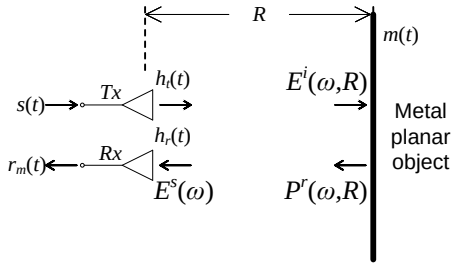

Fig. 2.1 Block diagram showing a metal planar object illuminated by a monostatic radar.

2.1.2 Target response of a Metal Planar Object

As indicated above, the target response of a metal planar object, $m(t)$, relates the scattered power and incident electric field at the metal surface. The relationship can be established by using the conventional radar cross section (RCS) of the object in

frequency domain. For practical purposes, the RCS of the metal planar object [48] can be defined as follows if the antennas are placed in the far-field region of the object:

$$\sigma = 4\pi R^2 \frac{\left|E^s(\omega)\right|^2}{\left|E^i(\omega, R)\right|^2} \tag{2.1}$$

and

$$W^s(\omega) = \frac{1}{2\eta}\left|E^s(\omega)\right|^2 = \frac{P^r(\omega, R)}{4\pi R^2} \tag{2.2}$$

where $W^s(\omega)$ is the scattered power density on the aperture of the Rx antenna, η is the wave impedance in free-space. $M(\omega)$, which is the Fourier transform of the target response of the object, $m(t)$, is defined as follows:

$$\left|M(\omega)\right| = \sqrt{P^r(\omega, R) \Big/ \frac{1}{2\eta}\left|E^i(\omega, R)\right|^2} \tag{2.3}$$

From (2.1)–(2.3), we can derive

$$\left|M(\omega)\right| = \sqrt{\sigma} \tag{2.4}$$

In addition, [59] showed that, when a rectangular metal plate is placed perpendicular to the direction of wave propagation, its RCS can be simplified as

$$\sigma = 4\pi \frac{A^2}{\lambda^2} \tag{2.5}$$

where A is the physical area of the plate, and λ is the wavelength. Eqn. (2.4) can be simplified as

$$\left|M(\omega)\right| = 2\sqrt{\pi}\frac{A}{\lambda} \tag{2.6}$$

Here we can establish the relationship between the amplitude of $M(\omega)$ and the physical area of the object. However, the phase of $M(\omega)$ has to be derived to fully characterize the target response of the metal planar object. Based on the relationship between the scattered electric fields in far-field region and the incident

fields on the planar object [60], the target response of the planar object can be written as

$$M(\omega) = -j \cdot 2\sqrt{\pi}\,\frac{A}{\lambda} \tag{2.7}$$

In time domain,

$$m(t) = -\frac{A}{c \cdot \sqrt{\pi}}\,\frac{d}{dt} \tag{2.8}$$

2.1.3 Transfer Function of UWB Antennas in Tx and Rx modes

Transfer functions of UWB antennas have been investigated in [61-63]. For the transmitting-receiving antenna system shown in Fig. 2.2, two identical UWB antennas are placed face-to-face to form a boresight antenna measurement system. The Tx antenna is excited with a UWB pulse, $s(t)$, while the Rx antenna is terminated with a 50 ohm load. $r(t)$ is the received pulse measured at the load. $S(\omega)$ and $R(\omega)$ are the Fourier transforms of $s(t)$ and $r(t)$ respectively. $E^i(\omega,R)$ is the electric field on the aperture of the Rx antenna. R is the distance between the Tx and Rx antennas. R is selected in such a way that it ensures far field conditions.

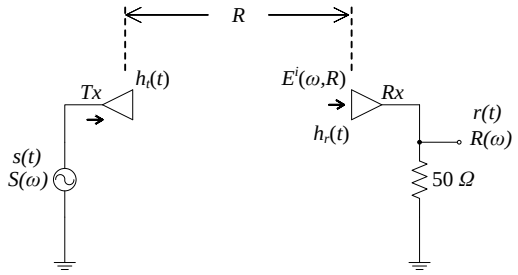

Fig. 2.2 Block diagram of a boresight antenna measurement system.

The transfer function of the antennas in Tx and Rx modes are defined as follows [64]:

$$H_T(\omega) = \frac{E^i(\omega,R)}{S(\omega)} \cdot R \cdot e^{jkR} \tag{2.9}$$

$$H_R(\omega) = \frac{R(\omega)}{E^i(\omega,R)} \tag{2.10}$$

where k is the wave number in free-space.

Furthermore, the transfer function of the entire antenna measurement system can be defined as

$$H(\omega, R) = \frac{R(\omega)}{S(\omega)} \tag{2.11}$$

Substituting $R(\omega)$ in (2.9) and $S(\omega)$ in (2.10) into (2.11), we can rewrite $H(\omega,R)$ as

$$H(\omega, R) = H_T(\omega) \cdot H_R(\omega) \cdot \frac{1}{R} \cdot e^{-jkR} \tag{2.12}$$

The relationship between $H_T(\omega)$ and $H_R(\omega)$ has been derived in [65] as

$$H_T(\omega) = \frac{1}{2\pi c} \cdot j\omega \cdot H_R(\omega) \tag{2.13}$$

Based on (2.12) and (2.13), we can derive

$$H_T(\omega) = \sqrt{\frac{1}{2\pi c} \cdot j\omega \cdot H(\omega, R) \cdot R \cdot e^{jkR}} \tag{2.14}$$

$$H_R(\omega) = \sqrt{2\pi c \cdot \frac{1}{j\omega} \cdot H(\omega, R) \cdot R \cdot e^{jkR}} \tag{2.15}$$

Once the excitation and received pulses of the antenna measurement system are measured, the transfer function of the UWB antennas can be estimated. By applying the inverse Fourier transform, the transfer function of the UWB antennas, $h_t(t)$ and $h_r(t)$, can be found.

2.1.4 Derivation of the Scattered Pulse from a Metal Planar Object

Using the target response of the metal planar object, $M(\omega)$, and the transfer function of the UWB antennas ($H_T(\omega)$ and $H_R(\omega)$), we can derive the received pulse, $R_m(\omega)$ (c.f. Fig. 2.1) as

$$R_m(\omega) = \frac{1}{2\sqrt{\pi}R^2} \cdot H_T(\omega) \cdot H_R(\omega) \cdot M(\omega) \cdot S(\omega) \cdot e^{-2jkR} \tag{2.16}$$

In time domain,

$$r_m(t) = \frac{1}{2\sqrt{\pi}R^2} \cdot h_t(t) * h_r(t) * m(t) * s(t - \frac{2R}{c}) \qquad (2.17)$$

2.1.5 Experimental Setup and Results

To verify the proposed method of predicting the amplitude and shape of the scattered pulse from a metal planar object, several experiments have been conducted. Estimation of the transfer function of the UWB antennas requires the knowledge of the system transfer function, $H(\omega,R)$. Fig. 2.3 shows the measurement setup to estimate the transfer function of the system. Two identical Vivaldi antennas [66] are placed in boresight (c.f. Fig. 2.3).

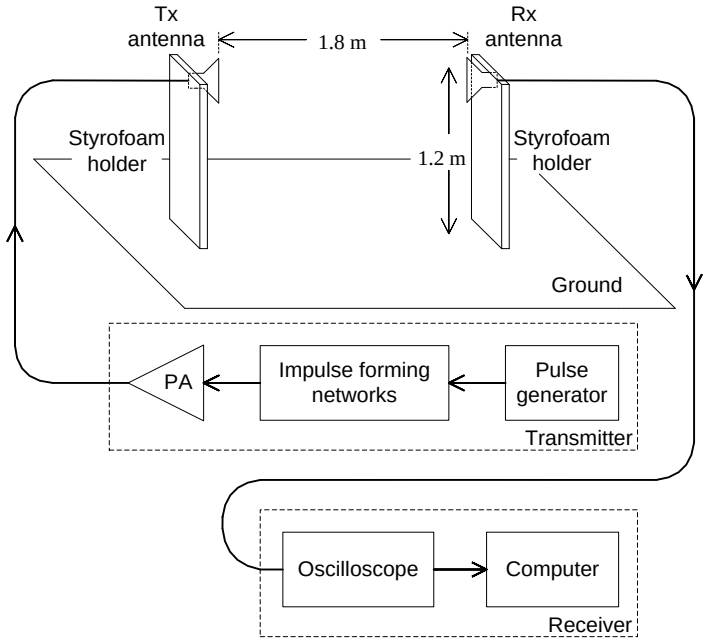

Fig. 2.3 Boresight antenna measurement setup to derive the transfer function of UWB antennas in Tx and Rx modes

The distance between the antennas is 1.8 m. Two Styrofoam holders support the antennas at a height of 1.2 m above the ground. The distance between the antennas and the ground ensures that the reflections from the ground can be time-gated. The transmitter consists of a step generator, two impulse forming networks (IFNs) and a power amplifier (PA). The pulse generator (AVTECH AVP-3SA-C) generates a train of 10 V, 50 ps rise-time steps at 1 MHz pulse repetition frequency (PRF). Two

IFNs (PSPL 5210) shape the generated step to first time derivative Gaussian pulse. The pulse is amplified by a PA (Hittite HMC659LC5) to a peak-to-peak voltage of 5.454 V. The excitation pulse and its frequency spectrum are shown in Fig. 2.4. The gain of the Vivaldi antennas and the equivalent isotropically radiated power (EIRP) of the excitation pulse are also shown in Fig. 2.4. From the EIRP profile, the center frequency of the pulse is 7 GHz.

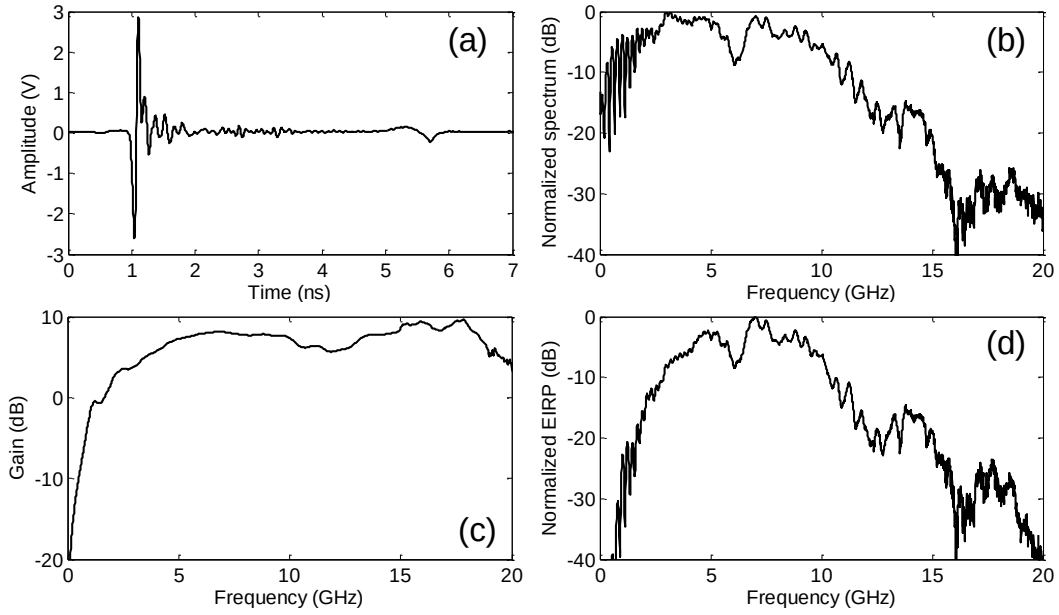

Fig. 2.4 Excitation pulse. (a): the time domain signal $s(t)$, (b): frequency components of $s(t)$, (c): antenna gain and (d): EIRP of the excitation pulse.

The UWB radar receiver consists of a sampling oscilloscope (Agilent DCA 86100B) that samples the signal at 40 GS/s. Time averaging is performed on the received pulses to improve the signal-to-noise ratio (SNR). The received pulse is post processed, as described above, to estimate the transfer function of the antennas in Tx and Rx modes.

The dimension of the Vivaldi antenna is 80 X 80 mm^2. Therefore the far-field region starts at 0.3 m from each antenna [48], so the distance of 1.8 m between the

two antennas ensures far-field conditions. The normalized measured pulse $r(t)$ is shown in Fig. 2.5. The first and second time derivatives of $r(t)$ are also shown in the same figure. The time axis and amplitude reference value in Fig. 2.5 are shifted for illustration purpose.

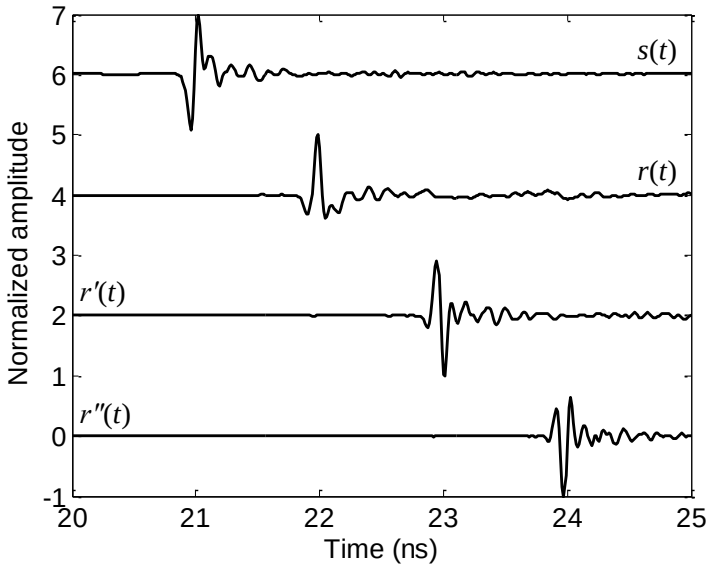

Fig. 2.5 Normalized pulses of the boresight antenna measurement. $s(t)$: the excitation pulse. $r(t)$: the measured received pulse. $r'(t)$: first time derivative of the measured received pulse. $r''(t)$: second time derivative of the measured received pulse (time axis is shifted for illustration purpose).

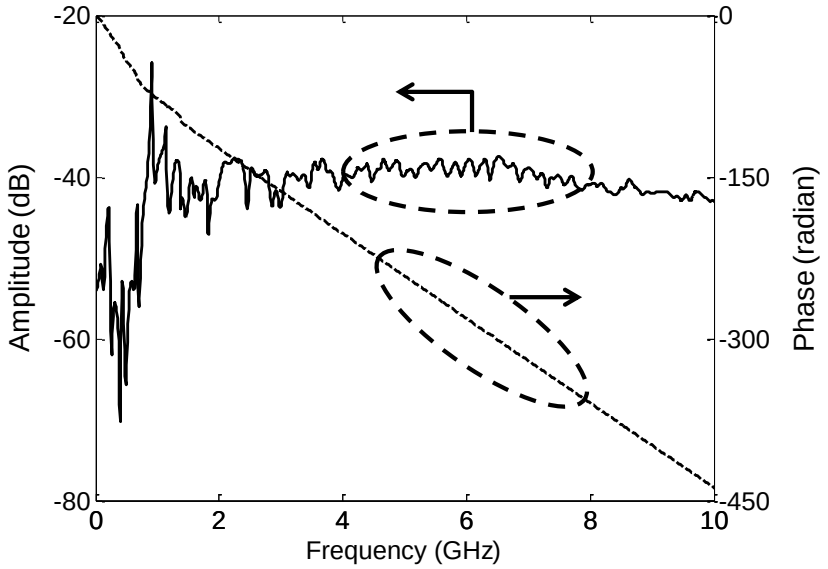

Fig. 2.6 Transfer function of the boresight antenna measurement system $H(\omega)$.

The transfer function of the entire measurement system, $H(\omega)$, is computed using the measured $s(t)$ and $r(t)$ as described in (2.11), the amplitude and phase of $H(\omega)$ is shown in Fig. 2.6. Based on the transfer function of the measurement system, using (2.14) and (2.15), the transfer function of the Vivaldi antennas, $h_t(t)$ and $h_r(t)$ are derived and shown in Fig. 2.7.

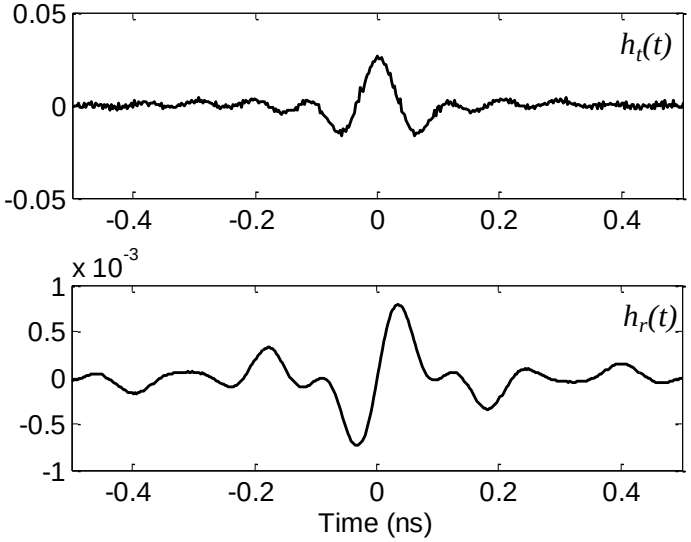

Fig. 2.7 Transfer function of the Vivaldi antennas in Tx (upper) and Rx modes (lower)

Characteristics of the pulse scattered from the metal planar objects can be estimated based on the target response of the metal planar object and transfer function of Tx and Rx antennas derived above. Here, we compare the measured and the estimated scattered pulse from a planar metallic object. The experimental setup is shown in Fig. 2.8. In Fig. 2.8 the Tx and Rx antennas are placed side-by-side, at 80 mm apart, to form a monostatic radar configuration. A metal planar object is supported by a Styrofoam holder at 1.2 m height. The distance between the metal planar object and the monostatic radar, R, ensures far-field conditions. In this experiment Vivaldi antennas are used as Tx and Rx antennas, and the dimension of the antennas is 80 X 80 mm^2, while the size of the metal object is 200 X 200 mm^2. Since the metal object is larger than the Vivaldi antennas, we should compute the far-field distance based

on the size of the object. The EIRP of the excitation pulse (c.f. Fig. 2.4), shows the center frequency of the pulses is 7 GHz, based on the center frequency the far-field distance is 3.73 m.

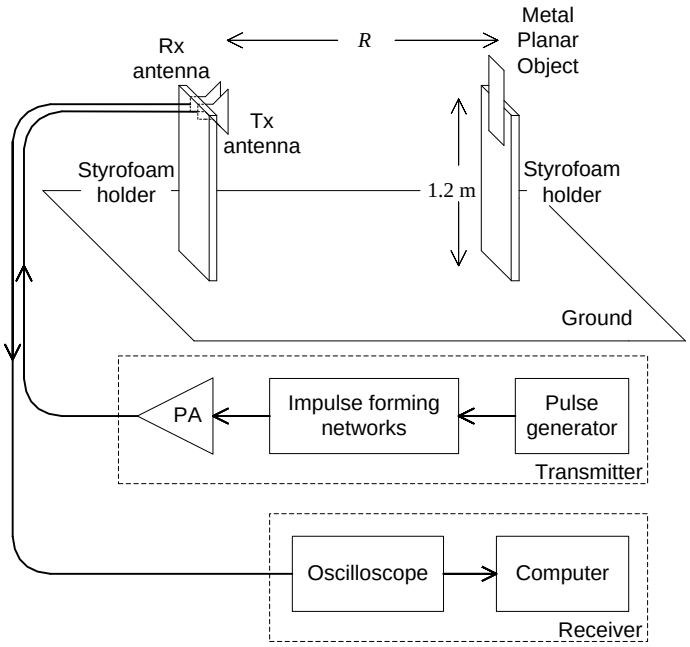

Fig. 2.8 A monostatic radar configuration to measure a UWB pulse scattered from a metal planar object

In the experimental setup shown in Fig. 2.8 the Tx and Rx antennas are placed close to each other, therefore the antenna coupling has to be accounted while estimating the scattered pulse. The effect of the antenna coupling can be eliminated by calibration. First, we measure the pulse received by the Rx antenna, $r_a(t)$, without any object in front of the radar. This measurement contains signals due to antenna coupling and other nearby scatterers. Then, the scattered pulse, $r_m(t)$, is measured after placing a 200 X 200 mm^2 metal planar object as shown in Fig. 2.8. The antenna coupling and the interference from all the nearby scatterers can be eliminated by subtracting $r_a(t)$ from $r_m(t)$. Let the calibrated scattered pulse be defined as $r_{mc}(t)$, where

$$r_{mc}(t) = r_m(t) - r_a(t) \tag{2.18}$$

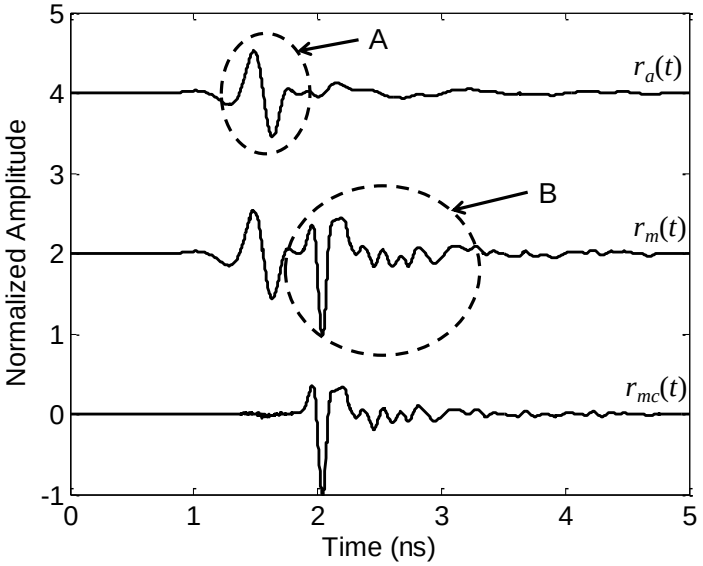

Fig. 2.9 Normalized received pulses from a metal planar object (200 X 200 mm^2) for monostatic radar configuration. $r_a(t)$: the received pulse in the absence of the object. $r_m(t)$: the received pulse in the presence of the object. $r_{mc}(t)$: the calibrated received pulse in the presence of the object.

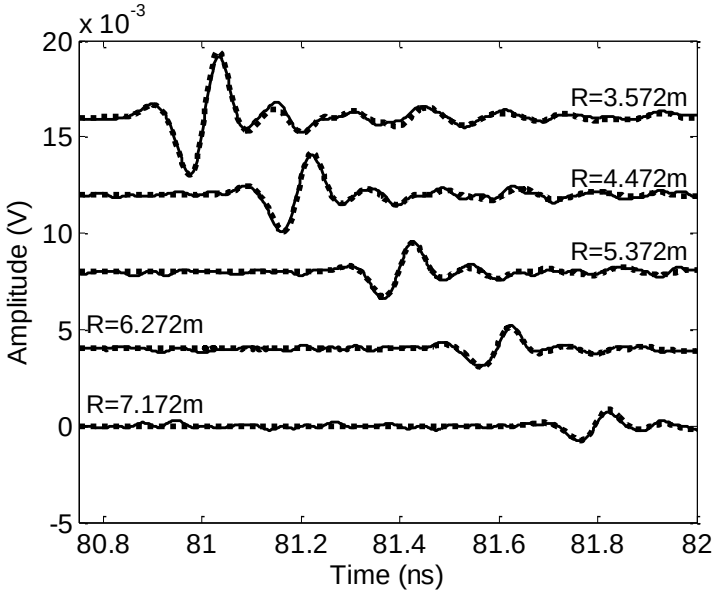

Fig. 2.10 Measured pulses scattered from a metal planar object (200 X 200 mm^2) at different distances (solid). The estimated scattered pulses (dotted) from equation (2.17) are also shown for comparison (time axis is shifted for illustration purposes)

Fig. 2.9 shows the calibrated received pulses. Measured $r_a(t)$ shows that some energy of the excitation pulse is coupled to the Rx antenna at 1.6 ns (Fig. 2.9:

'A').The scattered energy from the metal planar object is visible in $r_m(t)$ at 2.05 ns (Fig. 2.9: 'B'). $r_{mc}(t)$ is the calibrated scattered pulse from the object.

The measured scattered pulses from the metal planar object (200 X 200 mm^2) placed at different distances in far-field are shown in Fig. 2.10. The estimated scattered pulses by (2.17) are plotted in the same figure to show the accuracy of the modeling. We have also verified the scattered pulses from metal objects of sizes 100 X 100 mm^2 and 160 X 160 mm^2. In all the cases we found excellent agreement between the theory and measurements.

2.2 Transition of Pulse Shape in Near Field

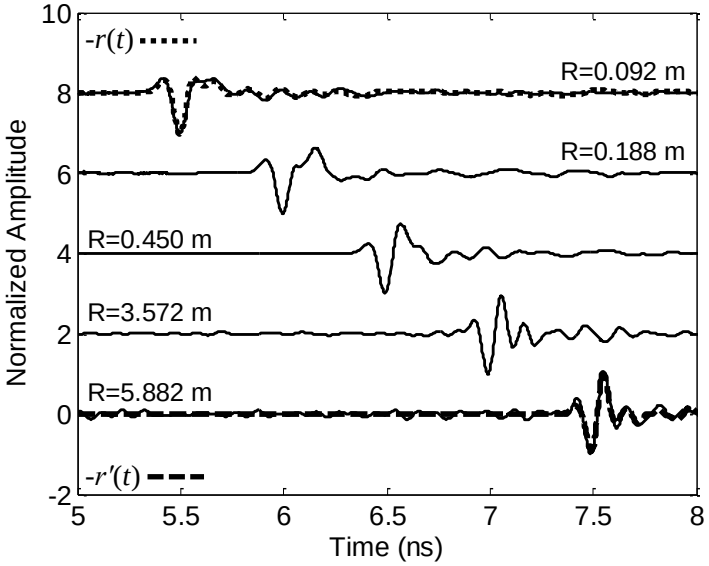

Fig. 2.11 Normalized measured pulses scattered from a metal planar object (200 X 200 mm^2) at different distances.

In this section we study the scattered pulse in the near-field region. The experimental setup is similar to that shown in Fig. 2.8. However the distance R between the object and the radar is decreased. The measured scattered pulses, after calibration, are shown in Fig. 2.11. It is clearly evident in Fig. 2.11 that the pulse

shape changes with distance in the near-field region. Fig. 2.11 also compares the measured scattered pulse with the inverted incident pulse ($-r(t)$) and its time derivative ($-r'(t)$). $-r(t)$ is the inverted received pulse of boresight antenna measurement system shown in Fig. 2.2.

Comparison shows that very close to the object the scattered pulse shape is same as that of the inverted incident pulse. In the far-field, the scattered pulse shape is same as that of the time derivative of the inverted incident pulse.

To study the distinction between the scattered pulses in near- and far-field regions of a UWB system, we calculate their fidelity factors [67]. The fidelity factor ($\mathcal{F}$) between two signals, say $a(t)$ and $b(t)$, has been defined in [67] as

$$\mathcal{F}\left[a(t), b(t)\right] = \max \int_{-\infty}^{\infty} a_n\left(t\right)\, b_n\left(t+\tau\right) dt \tag{2.19}$$

where $a_n(t)$ and $b_n(t)$ are the normalized $a(t)$ and $b(t)$,

$$a_n(t) = a(t) \Big/ \sqrt{\int_{-\infty}^{\infty} \left|a(t)\right|^2 dt} \tag{2.20}$$

$$b_n(t) = b(t) \Big/ \sqrt{\int_{-\infty}^{\infty} \left|b(t)\right|^2 dt} \tag{2.21}$$

The fidelity factors of the following cases are computed: the measured scattered pulse with the inverted incident pulse, i.e. $\mathcal{F}[r_m(t), -r(t)]$ and the measured scattered pulse with the inverted time derivative incident pulse, i.e. $\mathcal{F}[r_m(t), -r'(t)]$. For a 200 X 200 mm^2 metal planar object placed at different distances, the fidelity factors $\mathcal{F}[(r_m(t),-r(t)]$ and $\mathcal{F}[r_m(t),-r'(t)]$ are plotted in Fig. 2.12. The above fidelity factors are curve fitted to show their trends. From Fig. 2.12, it is clear that when the distance between the object and monostatic radar is 0.10 m, $\mathcal{F}[r_m(t),-r(t)]$ is as high as 0.96, that shows good fidelity between $r_m(t)$ and $-r(t)$. When the distance

between the object and the radar is larger, $\mathcal{F}[r_m(t),-r(t)]$ becomes less, and reaches a constant value of 0.79, showing less fidelity between them. On the other hand, when the distance is 0.10 m, $\mathcal{F}[r_m(t),-r'(t)]$ is as low as 0.74. $\mathcal{F}[r_m(t),-r'(t)]$ increases with the distance and reaches an average value of 0.95, showing good fidelity between $r_m(t)$ and $-r'(t)$. The decline of $\mathcal{F}[r_m(t),-r'(t)]$ in the far-field region is due to reduced signal-to-noise ratio (SNR) of $r_m(t)$.

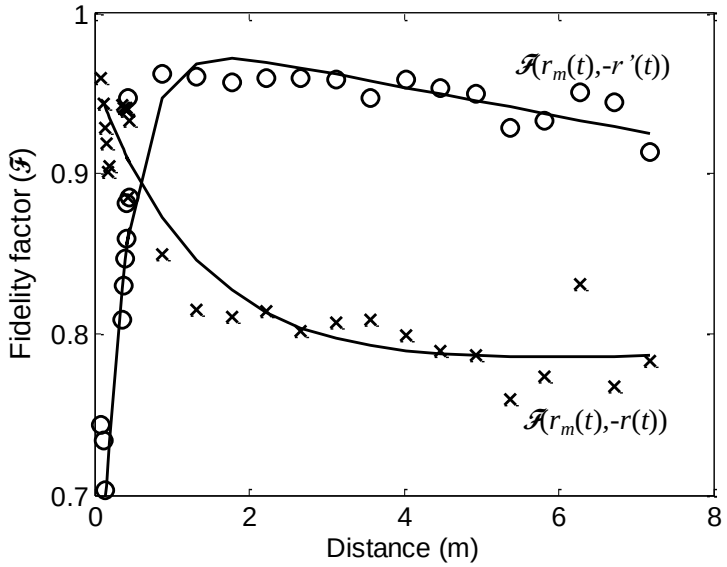

Fig. 2.12 A plot showing the fidelity between $r_m(t)$ and $-r(t)$ ('x'), $r_m(t)$ and $-r'(t)$ ('o') at different distances.

2.3 Effect of Multiple Scattering on UWB Pulse

In section 2.1 and 2.2, it was observed that the scattered pulse from a metal planar object, placed beyond a certain distance, is the time derivative of the inverted incident pulse. So, it is logical that a pulse scattered twice by metal planar objects would be the second time derivative of the incident pulse. In this section, we would like to confirm this phenomenon by conducting experiments. To measure the pulse that is scattered twice by metal planar objects, we conducted two experiments as shown in Fig. 2.13 and Fig. 2.14.

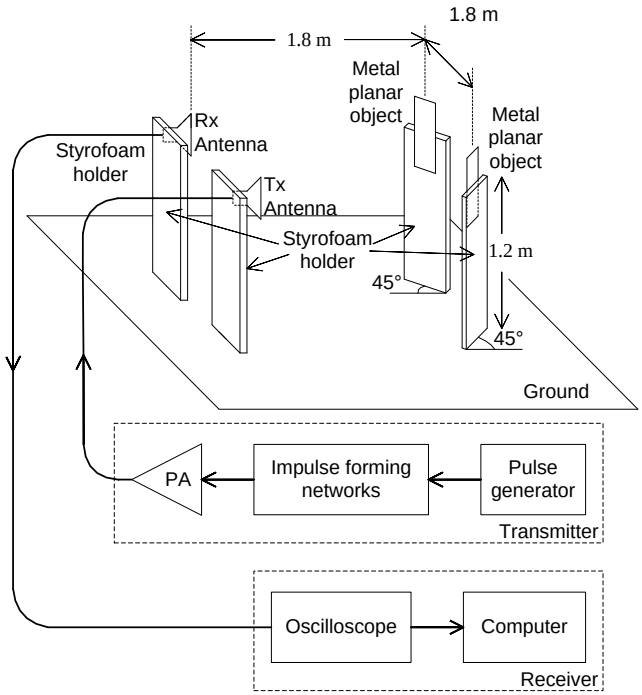

Fig. 2.13 Experimental setup to study the effect of multiple scattering on UWB pulse with bi-static radar configuration.

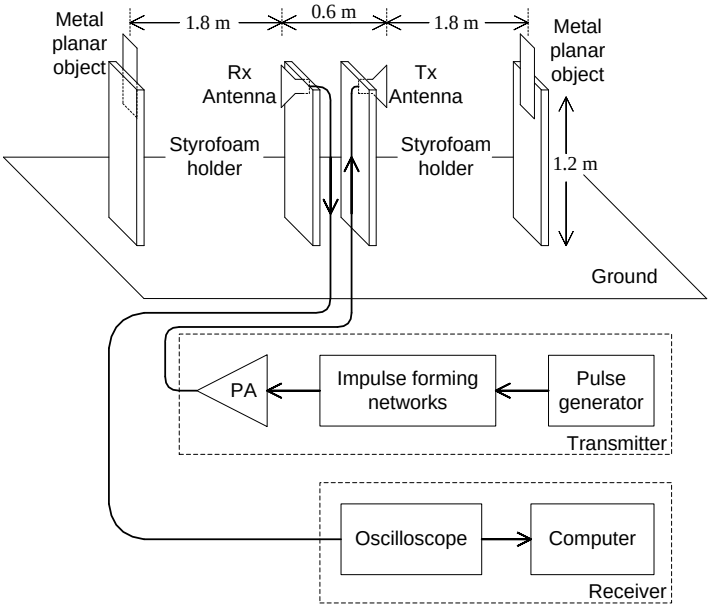

Fig. 2.14 Experimental setup to study the effect of multiple scattering on UWB pulse with back-to-back radar configuration.

As shown in Fig. 2.13, two identical Vivaldi antennas are placed side-by-side at 1.8 m separation, to satisfy far-field condition, to form a bi-static radar configuration. The antennas are placed 1.2m above the ground. A 200 X 200 mm^2 metal planar object is placed in front of the Tx antenna with a 45 °angle between the propagation direction and the surface of the object. A second metal planar object (160 X 160 mm^2) is placed in front of the Rx antenna with a 45 °angle between the propagation direction and the surface of the object. The distances between the objects and the bi-static radar are 1.8 m.

In Fig. 2.14, two identical Vivaldi antennas are placed back-to-back. The distance between the antennas is 0.6 m. Two metal planar objects (200 X 200 mm^2 and 160 X160 mm^2) are placed at 1.8m away from the Tx and Rx antennas respectively. In both the experiments, the UWB pulse radiated by the Tx antenna impinges on the first object (200 X 200 mm^2) and scattered into space. The scattered pulse is then intercepted by the second object (160 X 160 mm^2) and is received by the Rx antenna.

The normalized received pulses for bi-static radar configuration, $r_{bs}(t)$, and for back-to-back configuration, $r_{bb}(t)$, are plotted in Fig. 2.15. For comparison the second time derivative of the incident pulse $r''(t)$ is also plotted in the same figure. The fidelity factor between $r_{bs}(t)$ and $r''(t)$ is 0.92, while the fidelity factor between $r_{bb}(t)$ and $r''(t)$ is 0.95. The high value of the computed fidelity factors confirms that the pulse scattered twice by metal planar objects would be the second time derivative of the incident pulse.

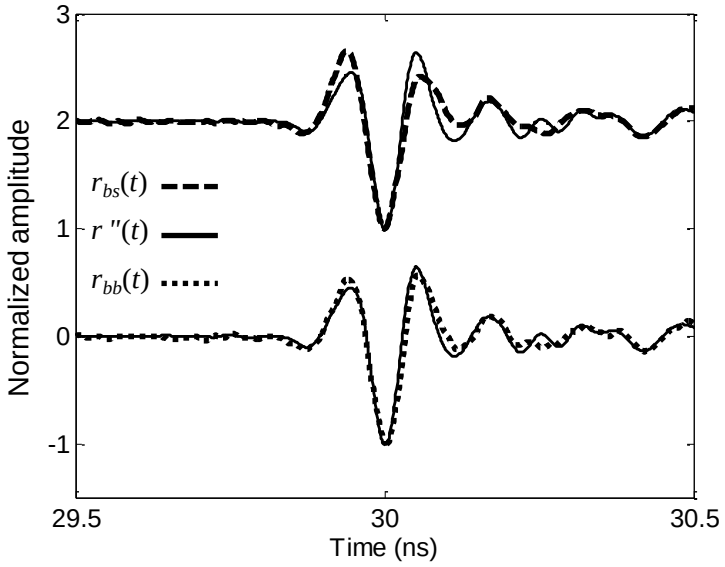

Fig. 2.15 Normalized measured pulses scattered from two metal planar objects for bi-static radar configuration (dash) and back-to-back radar configuration (dotted). The second derivative of the incident pulse (solid) is also shown for comparison.

2.4 Frequency-Averaged Radar Cross Section

2.4.1 Overview

In previous sections scattered pulse from a metal planar object has been studied, i.e. the amplitude and shape of the scattered pulse in far-field region is computed. In this section we define and study the frequency-averaged radar cross section (RCS) of an object based on scattered pulse characteristics. The frequency-averaged RCS addresses the lack of direct methods in estimating the objects' conventional RCS in pulsed based UWB radar measurements. In this section, we want to show that the proposed frequency-averaged RCS value is same as the conventional RCS. This allows us to compute the scattered pulse energy based on the conventional RCS of the object for UWB radar applications. The closed form equation of the frequency-averaged RCS of an object is defined in terms of the antenna effective height, and the energy of the excitation and received pulses. A block diagram of the RCS measurement is shown in Fig. 2.16. $s(t)$ and $r_m(t)$ are the excitation and

received pulses respectively; l_{et} and l_{er} are the effective height of the antennas in Tx and Rx modes. The distance between the object and the antennas is R. U^i is the energy density of the pulse incident on the object, and U^s is the scattered energy density on the aperture of the Rx antenna. $\mathcal{E}^r$ is the scattered energy at the object surface. σ_{avg} is the frequency-averaged RCS that quantifies the energy intercepted by the object for a UWB pulse that is incident on its surface.

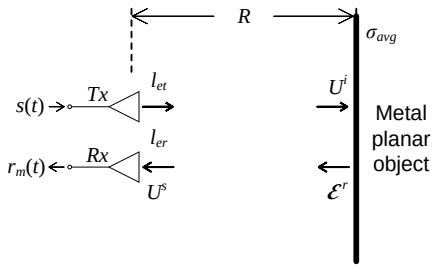

Fig. 2.16 Block diagram to estimate the frequency-averaged RCS (σ_{avg}) of a metal planar object.

2.4.2 Effective Height of Vivaldi Antenna

The effective height of an antenna is a measure of focusing or accepting the energy in the Tx or Rx modes under matched polarization [68]. On the other hand, [69] shows that the path loss for UWB pulse propagation is $1/4\pi R^2$, which is independent of frequency. As described in [68], when a metal planar object is placed in far-field of an antenna, the energy density incident on the object, U^i, is

$$U^i = \frac{\mathcal{E}_t \cdot l_{et}}{4\pi R^2} \tag{2.22}$$

where l_{et} is the effective height of the antenna in Tx mode, $\mathcal{E}_t$ is the energy of the excitation pulse that can be calculated as

$$\mathcal{E}_t = \int_{-\infty}^{\infty} |s(t)|^2 \, dt \tag{2.23}$$

Similarly, the relationship between the scattered energy $\mathcal{E}^r$ by the object and the energy density U^s that impinges on the aperture of the Rx antenna is:

$$U^s = \frac{\mathcal{E}^r}{4\pi R^2} \tag{2.24}$$

Furthermore, the received energy by the antenna is directly proportional to the effective height of the antenna. The relationship between the energy density of the pulse that impinges on the aperture of the Rx antenna and the received pulse energy is

$$\mathcal{E}_s = U^s \cdot l_{er} \tag{2.25}$$

where l_{er} is the effective height of the antenna in Rx mode, $\mathcal{E}_s$ is the energy of the received pulse:

$$\mathcal{E}_s = \int_{-\infty}^{\infty} |r_m(t)|^2 \, dt \tag{2.26}$$

2.4.3 Closed-Form Approximation of the Frequency-Averaged RCS

The frequency-averaged RCS (σ_{avg}) is defined as the ratio of the scattered energy by the object ($\mathcal{E}^r$) to the impinging energy density (U^i), shown in Fig. 2.16,

$$\sigma_{avg} = \frac{\mathcal{E}^r}{U^i} \tag{2.27}$$

According to (2.22)−(2.27), the frequency-averaged RCS can be expressed in terms of the effective height of the antennas, the excitation, and the received pulse energies:

$$\sigma_{avg} = \frac{\mathcal{E}_s}{\mathcal{E}_t} \cdot \frac{\left(4\pi R^2\right)^2}{l_{er} \cdot l_{et}} \tag{2.28}$$

2.4.4 Experimental Setup and Results

We conduct experiments to measure the frequency-averaged RCS of a metal planar object with UWB pulses. The experimental setup is similar to that shown in Fig. 2.8. The effective height of the antenna is defined as described in [68]. The structure of the antennas used in this experiment is shown in Fig. 2.17.

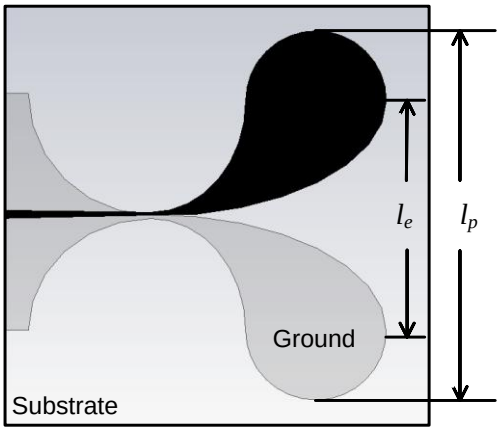

Fig. 2.17 Physical height (l_p) and effective height (l_e) of the Vivaldi antennas.

The physical height of the antenna, l_p, is 80 mm and its effective height, l_e, for 70% radiation efficiency, is 56 mm. Since we use identical Vivaldi antennas in Tx and Rx modes, l_{er} is equal to l_{et}.

In this experiment we have computed the frequency-averaged RCS for three different metal planar objects of sizes 100 X 100 mm^2, 160 X 160 mm^2 and 200 X 200 mm^2 respectively. In each computation, we have measured the scattered pulse at various distances from the object. Signal-to-noise ratio (SNR) of the measured pulse worsens with increasing distance; hence to minimize the noise in measurements, the received pulse is filtered.

Based on the antenna operating frequency and frequency spectrum of the excitation pulse, bandwidth of the filter is selected as shown in Fig. 2.18(a). Fig. 2.18(b) shows the effect of filtering on the received pulse that is scattered from a metal planar object (200 X 200 mm^2) at 7.17 m. Furthermore, to minimize the effect of the noise, the integration time in this computation is set to 1ns, i.e. 0.5 ns before and after the time-of-arrival (TOA) of the received pulse. The TOA is determined from its zero crossing, as shown in Fig. 2.18(b).

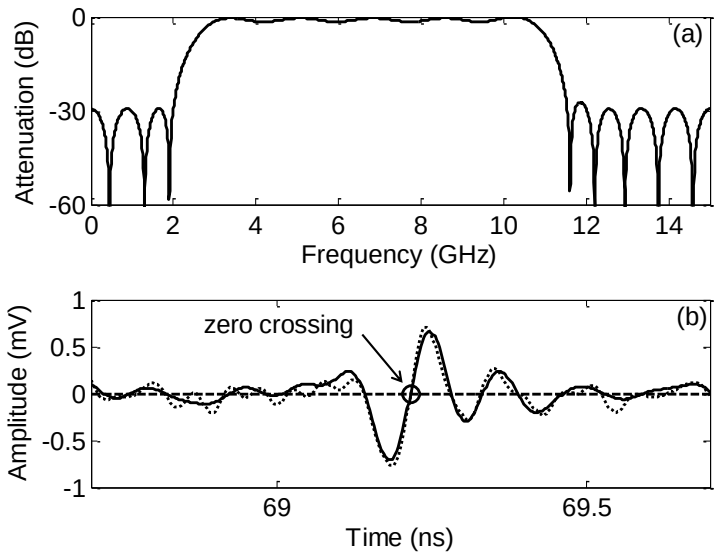

Fig. 2.18 Band-pass filter employed in this work. (a): Frequency response. (b): Filtering effect (dotted: without BPF, solid: with BPF) on the received pulse scattered from a metal planar object (200 X 200 mm^2) at 7.172 m.

The frequency-averaged RCS (σ_{avg}) computed by (2.28) at different distances are plotted in Fig. 2.19, Fig. 2.20 and Fig. 2.21 for metal planar objects of different sizes.

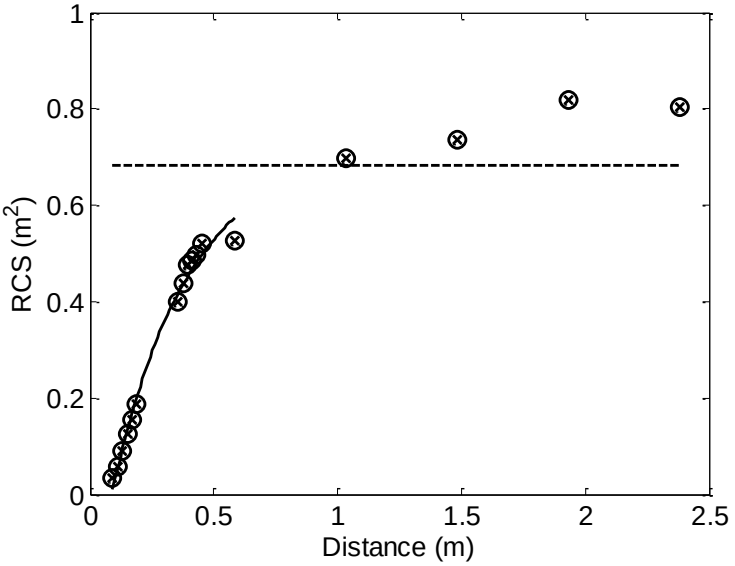

Fig. 2.19 The frequency-averaged RCS ('x') of a 100 X 100 mm^2 metal planar object in comparison with the conventional RCS (dash).

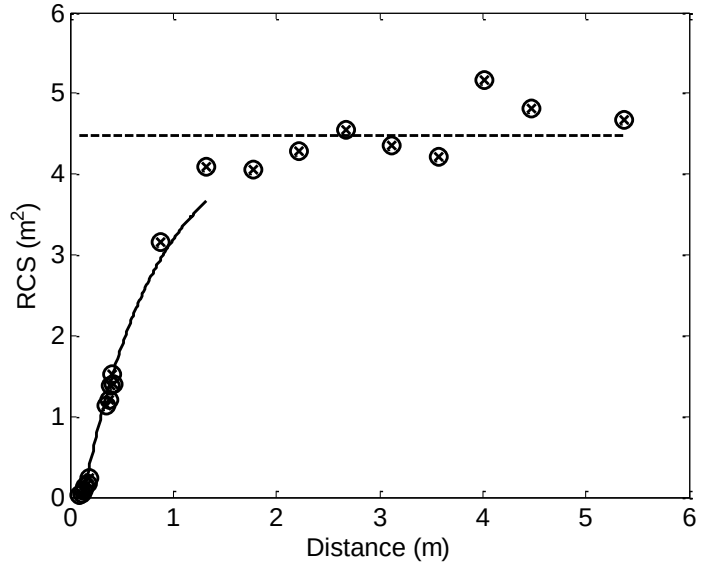

Fig. 2.20 The frequency-averaged RCS ('x') of a 160 X 160 mm^2 metal planar object in comparison with the conventional RCS (dash).

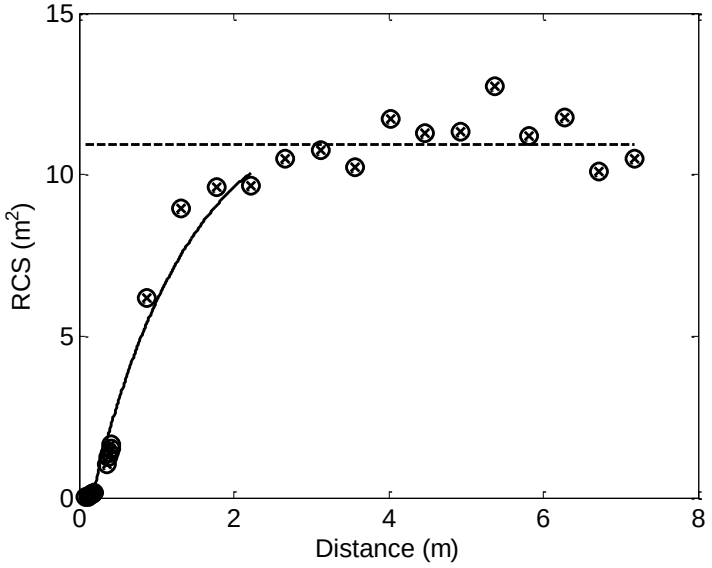

Fig. 2.21 The frequency-averaged RCS ('x') of a 200 X 200 mm^2 metal planar object in comparison with the conventional RCS (dash).

To validate the proposed equation (2.28), the conventional RCS defined in (2.5), at 7 GHz, is also plotted. In the near-field region [48], data is curve fitted to show the trend. In the far-field region, the frequency-averaged RCS shows noticeable fluctuations at higher distances especially for the case of 100 X 100 mm^2 metal

planar object. The fluctuations are due to the deteriorating SNR of the received pulse. It is noticed that the measured frequency-averaged RCS of the objects increases in the near-field, while it is almost constant in the far-field. The arithmetic mean of the computed RCS in the far-field is very close to the conventional values as shown in TABLE 2.1. From TABLE 2.1, it can be observed that the proposed frequency-averaged RCS values, in the far-field region, are close to the conventional RCS values. These results enable us to reliably compute the scattered pulse energy based on the conventional narrowband RCS of the object for UWB radar applications.

TABLE 2.1 FREQUENCY-AVERAGED RCS (σ_{avg}) AND CONVENTIONAL RCS OF METAL PLANAR OBJECTS.

Metal planar object size (mm^2)	Arithmetic mean of σ_{avg} (m^2)	Conventional RCS (m^2)	Difference (%)
100 X 100	0.76	0.68	11.11
160 X 160	4.54	4.48	1.33
200 X 200	11.10	10.95	1.36

2.5 Summary

In this chapter, we proposed a method of estimating the received UWB pulse scattered from a metal planar object in far-field. Estimated received pulses are in good agreement with the measurements in terms of amplitude and shape. When the object is placed in near-field, the transition of the received pulse shape is analyzed. Furthermore, a frequency-averaged RCS of the metal planar object is defined in terms of the effective height of the Tx and Rx antennas, and the energy of the excitation and received pulses. The proposed analysis allows us to compute the

scattered pulse shape and energy based on the conventional RCS of the object for UWB radar applications.[1]

[1] *A version of this chapter has been submitted for publication in IEEE Transactions on Antennas and Propagation.*

Chapter-III

3 Buried Object Characterization Using Ultra-Wideband Ground Penetrating Radar

Introduction

In this chapter, a method of characterizing buried non-magnetic objects in the ground using ultra-wideband (UWB) ground penetrating radar (GPR) is proposed. In this method, UWB pulses are radiated by the radar, while scattered pulses from the ground with the buried object are received. The received pulses are then post-processed to estimate the depth, thickness and electrical properties of the buried object. A constant depth and thickness is enforced at all frequencies while the signals are processed to extract the buried object characteristics, resulting in more accurate estimations and reduced processing time. In addition, path loss due to the close proximity of the radar to the ground is compensated analytically. On average, the proposed method can achieve object thickness accuracy of ± 0.7 mm and sufficient reliability in estimating the permittivity of buried objects for the purpose of material identification. Incorporating the proposed method into the GPRs enhances their existing imaging ability by adding material identification capability.

In our intended application, a monostatic UWB GPR is used to estimate the properties of buried objects that are encountered in the tunneling applications. Tunneling by the use of a tunnel boring machine (TBM) is hampered by buried objects such as pipes, rocks, boulders or other man-made objects. Boulders in soil tunneling and in micro tunneling have resulted in time and cost overruns such as

cutter discs deterioration and replacement and tunnel alignment. Current practices commonly rely on excavating a limited quantity of vertical boreholes during site investigation or taking coring samples at the tunnel face in order to acquire geotechnical data and probe any obstacles, which are time-consuming and expensive while failing to provide accurate and timely information as needed to characterize the boulders or man-made obstructions lying immediately ahead of the tunnel face. In this chapter we propose a method, using UWB GPR, to identify buried objects in the soil. This model can also be used to probe a wall with different layers of construction materials.

This chapter is organized as follows: In section 3.1, the method of estimating buried object characteristics using the received scattered pulses is described. The process involves matching the measured reflection coefficient with that from theoretical derivation. The depth, thickness and electrical properties of the buried object are estimated based on the best fit between the measured and theoretical reflection coefficient. The proposed algorithm is summarized in the system flowchart as shown in Section 3.2. Section 3.3 describes the experimental setup and measurement procedure to validate the proposed method. Using the measured scattered pulses in Section 3.3, the estimated physical and electrical properties of the buried object are presented and verified in Section 3.4.

3.1 Theory

3.1.1 Overview

In this section, a free-space method of estimating the physical and electrical properties of a buried object is described. The measurements to characterize the buried object are performed above the ground, in which scattered pulses from the

ground with the buried object are captured by the receiving (Rx) antenna. The Rx antenna is placed beside the transmitting (Tx) antenna in a monostatic radar configuration. Both the Tx and Rx antennas are directional to maintain an illumination area that is smaller than the transverse area of the buried object to eliminate edge effect. Therefore, the ground and the buried object can be assumed to be horizontally layered, or one-dimensional as shown in Fig. 3.1. For verification purpose in the experiments, the ground is terminated after a certain depth beneath the object.

As shown in Fig. 3.1, the Tx antenna is radiating onto the multilayered ground and buried object. Vivaldi antennas [66] are used as Tx and Rx antennas for our experiments. The five layers of different materials are labeled as '1' to '5'. Regions 1 and 5 are free-space, regions 2 and 4 are ground, while region 3 is the buried object. The Tx antenna is fed with a sub-nanosecond pulse, $s(t)$, radiating into free-space in region 1. The radiated pulse propagates onto the ground and is scattered by the ground with the buried object. Part of the scattered pulse propagates back and is received by the Rx antenna as $r(t)$. $r(t)$ is further analyzed to estimate the physical and electrical properties of the buried object.

The excitation and received pulses, $s(t)$ and $r(t)$, are pulse-shaped by Tx and Rx antennas respectively. This pulse shaping effect can be modeled by the transfer function of the antenna in Tx and Rx modes, $h_t(t)$ and $h_r(t)$ [63, 64, 70]. $G_t(\omega)$ and $G_r(\omega)$ are the band-limited antenna gain in Tx and Rx modes respectively. The dielectric property of the ground (ε_{r2} and ε_{r4}) can be evaluated separately, which are known quantities during the buried object estimation. Hence, the research problem is simplified as an estimation of the depth (d_2), thickness (d_3) and complex

dielectric permittivity (ε_{r3}) of the buried object. Due to practical reasons mentioned above, the depth of the ground after the buried object (d_4) is also estimated. $y_s(t)$ is the aggregate transfer function of the ground with the buried object, and will be derived in the next section. In addition, the derived $y_s(t)$ will be used to obtain the measured reflection coefficient of the ground with the buried object.

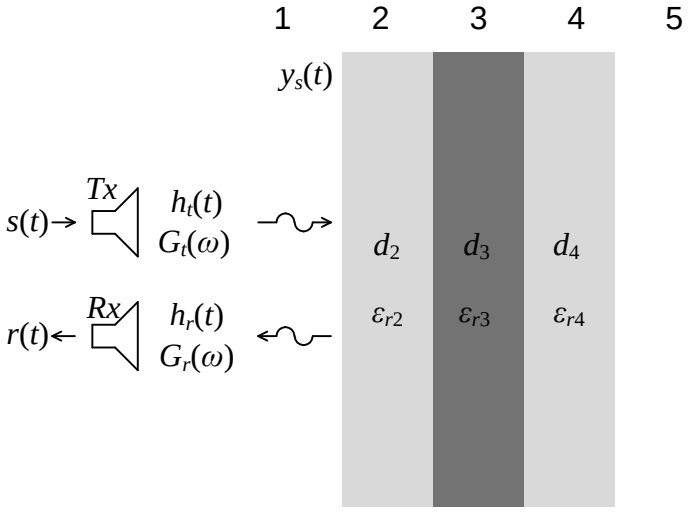

Fig. 3.1 Diagram showing a multilayered dielectric slab that models the ground depths (d_2 and d_4) and dielectric permittivity (ε_{r2} and ε_{r4}); buried object thickness (d_3) and dielectric permittivity (ε_{r3}) being investigated by the transmitting and receiving antennas of a UWB GPR.

3.1.2 Measured Reflection Coefficient of the Ground with the Buried Object

Although $r(t)$ contains the desired information of the ground and the buried object, undesired information such as the excitation pulse, antenna effect, antenna coupling and other reflections due to nearby scatterers (e.g. nearby radar fixtures and mounting vehicle) are also embedded in it. Hence, the first step is to decouple all the undesired information from the received pulse $r(t)$. To do that, two calibration measurements are conducted. First, the received pulse of the radar, $r_a(t)$, is measured in free-space without the presence of the ground or the buried object. Next, the received pulse of the radar, $r_m(t)$, is recorded with a large thin metal sheet placed on top of the ground. $r_s(t)$ is the total measured scattered pulse that includes

reflection from the ground with the object, Tx and Rx antenna direct coupling and reflections from nearby scatterers. $r_a(t)$ accounts for antenna coupling and reflections due to nearby scatterers. After accounting for the undesired signals, the measured pulses are

$$r_{sc}(t) = r_s(t) - r_a(t) \tag{3.1}$$

$$r_{mc}(t) = r_m(t) - r_a(t) \tag{3.2}$$

where $r_{sc}(t)$ and $r_{mc}(t)$ are the calibrated received pulses due to the ground with the buried object, and the large metal sheet respectively, i.e. eliminating antenna coupling and reflections due to nearby scatterers. Based on the analysis described in [63, 70], $r_{sc}(t)$ and $r_{mc}(t)$ can be decomposed as (c.f. Fig. 3.1)

$$r_{sc}(t) = s(t) * h_t(t) * F^{-1}\left[G_t(\omega)\right] * y_s(t) * F^{-1}\left[G_r(\omega)\right] * h_r(t) \tag{3.3}$$

$$r_{mc}(t) = s(t) * h_t(t) * F^{-1}\left[G_t(\omega)\right] * y_m(t) * F^{-1}\left[G_r(\omega)\right] * h_r(t) \tag{3.4}$$

where $h_t(t)$ and $h_r(t)$ are the transfer functions of the Tx and Rx antennas respectively; $y_s(t)$ and $y_m(t)$ are the transfer functions of the ground with the buried object, and metal sheet respectively; '*' denotes convolution. By Fourier transform of (3.3) and (3.4), the following ratio can be derived:

$$\frac{F\left\{r_{sc}(t)\right\}}{F\left\{r_{mc}(t)\right\}} = \frac{F\left\{r_s(t) - r_a(t)\right\}}{F\left\{r_m(t) - r_a(t)\right\}} = \frac{\Gamma_s(f)}{\Gamma_m(f)} \tag{3.5}$$

where $\Gamma_s(f)$ and $\Gamma_m(f)$ are the Fourier transforms of $y_s(t)$ and $y_m(t)$ respectively. Based on the observations in [70], $\Gamma_s(f)$ and $\Gamma_m(f)$ can be deemed as measured reflection coefficients of the ground with the buried object, and the metal sheet respectively.

$$\Gamma_s(f) = -\frac{F\left\{r_s(t) - r_a(t)\right\}}{F\left\{r_m(t) - r_a(t)\right\}} \tag{3.6}$$

In (3.6), $\Gamma_m(f)$ is replaced with -1 since it represents the reflection due to the

metal sheet which is assumed to be perfect electrical conductor (PEC) [48].

3.1.3 Theoretical Reflection Coefficient of the Ground with the Buried Object

In this section, theoretical reflection coefficient of the ground with the buried object is derived by using a transmission line analogy [71] as shown in Fig. 3.2. Each region in Fig. 3.1 is analogous to a section of the transmission line in Fig. 3.2. Using this analogy, instead of solving the electromagnetic scattering due to multiple discontinuities, standard transmission line equations [71] can be applied to derive the reflection coefficient of a multi-section transmission line.

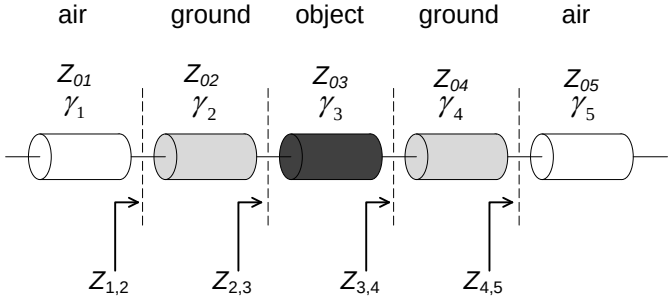

Fig. 3.2 Diagram showing the analogy between a multi-layer plane wave propagation and a multi-section transmission line.

The parameters in Fig. 3.2 are related to that of Fig. 3.1 as follows:

$$\gamma_k = j\,2\pi f \sqrt{\varepsilon_{rk}}\,/c \tag{3.7}$$

$$Z_{0k} = \eta_0 / \sqrt{\varepsilon_{rk}} \tag{3.8}$$

$$Z_{k,k+1} = Z_{0(k+1)} \frac{Z_{k+1,k+2} + Z_{0(k+1)} \tanh(\gamma_{k+1} d_{k+1})}{Z_{0(k+1)} + Z_{k+1,k+2} \tanh(\gamma_{k+1} d_{k+1})} \tag{3.9}$$

$$\Gamma_t(f) = \left(Z_{1,2} - Z_{01}\right) / \left(Z_{1,2} + Z_{01}\right) \tag{3.10}$$

γ_k and Z_{0k} are the propagation constant and characteristic impedance of the k-th section of the transmission line. γ_k and Z_{0k} are related to the dielectric property of the k-th layer as described in (3.7) and (3.8). $Z_{k,k+1}$ is the input impedance looking into the k+1th section from the k-th section. $Z_{k,k+1}$ is related to the parameters of the

multi-layered dielectric as described in (3.9). k = 1, 2, 3, 4 or 5 in (3.7)–(3.8), while k = 1, 2 or 3 in (3.9). $\Gamma_t(f)$ is the theoretical reflection coefficient of the ground with the buried object. Since region 5 extends to infinity, $Z_{4,5}=Z_{05}$. The other parameters in (3.7)–(3.10) are defined as follows: d_k is the thickness of the k-th medium; ε_{rk} is the relative permittivity of the k-th medium; c is the speed of light in free-space, and η_0 is the intrinsic impedance of free-space. The relative permittivity of the k-th medium, ε_{rk}, is a complex number, and can be expressed as $\varepsilon'_{rk} - j\varepsilon''_{rk}$, where ε'_{rk} and ε''_{rk} are the real and imaginary parts of the material′s relative permittivity. In (3.10), a relationship between the reflection coefficient of the ground with the buried object, and their physical and electrical parameters is established. In addition, if there is no measurement noise and assumption of plane wave propagation is met, theoretically derived $\Gamma_t(f)$ in (3.10) can be equated to the measured $\Gamma_s(f)$ in (3.6), and a simple solution can be found for the appropriate values of the buried object depth, thickness and dielectric properties. However, due to practical reasons such as the presence of measurement noise, inhomogeneous ground material, surface roughness and non-planar wave propagation, it is often infeasible to equate $\Gamma_t(f)$ with $\Gamma_s(f)$. Hence, parameter optimization techniques such as the mean square error (MSE) method [29, 44, 72] are used. In this method, averaging around the frequency of interest is implemented to reduce the possibility of incorrect estimation of physical and electrical properties due to above-mentioned non-ideal conditions.

3.1.4 MSE Method of Estimating Buried Object Parameters

Mean square error (MSE) method is an iterative algorithm that aims to find a set of physical and electrical parameters of the buried object by minimizing the absolute differences between the measured reflection coefficient, i.e. $\Gamma_s(f)$, and the theoretical reflection coefficient, i.e. $\Gamma_t(f)$. Let M_0 be the averaged absolute

difference between the measured and theoretical reflection coefficient for all possible combinations of physical and electrical properties:

$$M_0(d_2, d_3, d_4, f, \varepsilon'_{r3}, \varepsilon''_{r3}) = \frac{1}{2N+1} \sum_{i=-N}^{N} \left| \Gamma_s(f + i\Delta f) - \Gamma_t(d_2, d_3, d_4, f + i\Delta f, \varepsilon'_{r3}, \varepsilon''_{r3}) \right| \tag{3.11}$$

where d_2 and d_3 are the depth and thickness of the buried object; d_4 is the thickness of the ground beneath the object that needs to be estimated. ε'_{r3} and ε''_{r3} are real and imaginary parts of the relative dielectric permittivity of the buried object (ε_{r3}); f is the frequency, and Δf is the frequency step of the Fourier transform in (3.6). This optimization process involves finding a set of parameters that minimizes M_0. Averaging is applied for $2N$+1 reflection coefficient values centered at f to reduce the possibility of incorrect estimation of the physical and electrical properties due to non-ideals. The theoretical basis of doing this is that both ε'_r and ε''_r change gradually with respect to frequency. It can be noted that the frequency range of the estimation is slightly decreased due to the averaging effect.

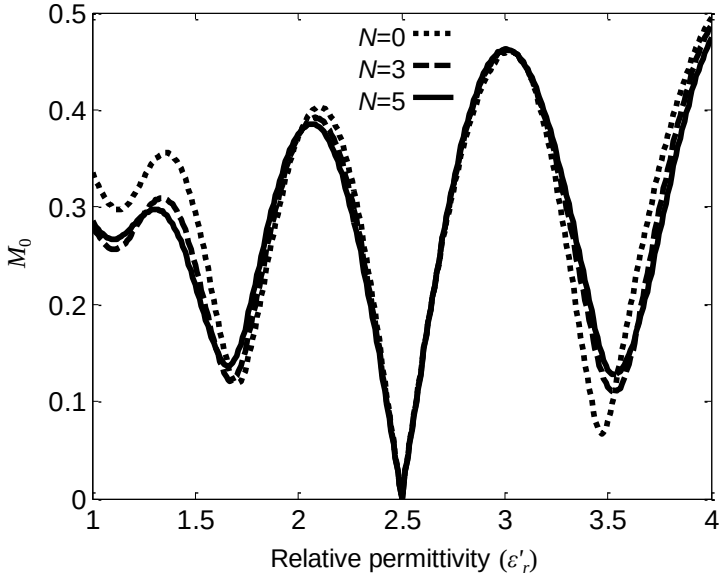

Fig. 3.3 A plot showing the averaging effect of N on M_0 of a mock sample (ε'_r =2.5, d = 0.1m) at 5 GHz

The averaging effect of N on M_0 of a dielectric sample (ε'_r =2.5, d = 0.1m) is shown in Fig. 3.3. In this illustration, N is selected to be zero (dotted), three (dashed) and five (solid) respectively.

It can be noted that when N =0, there is a global minimum M_0 of 0 at ε'_r =2.5 and three local minima M_0 of 0.297, 0.119 and 0.067 at ε'_r =1.13, 1.7 and 3.47 respectively. In reality, the local minima with low M_0 values may become global minima due to the measurement noise, inhomogeneous ground material, surface roughness and non-planar wave propagation. If this happens in the measurement, the relative dielectric permittivity will be incorrectly estimated to be 1.13, 1.7 or 3.47 instead of 2.5. To resolve this problem, we increase N to 3 and 5 and then check the value of M_0. When N is 5, the M_0 corresponding to local minima are changed to 0.267, 0.136 and 0.128 respectively. By doing this, the possibility of incorrect estimation of ε'_r is reduced since the difference between global minimum (0) and local minima (0.267, 0.136 and 0.128) become more distinct.

MSE methods reported in the existing literature perform parameter sweeps of the buried object depth, thickness and dielectric properties for all measured frequencies of $\Gamma_s(f)$. In (3.11), parameter sweeps involve varying d_2, d_3, d_4, f, ε'_{r3} and ε''_{r3}, resulting in a 6-dimensional matrix of possible solutions. Direct application of the MSE method of estimating the buried object parameters in our research problem has faced several difficulties: Firstly, the estimated depth and thickness of the buried object in one measurement is not constant with respect to frequency. In addition, for a few cases, their values vary drastically even after implementing averaging, which further affects the accuracy of the estimated electrical properties. Secondly, the size of the solution domain in the MSE method increases

exponentially with the increment of unknown parameters. Optimizing for depth and thickness of the buried object at each frequency is redundant and it unnecessarily slows down the process, since these parameters are independent of frequency.

A better approach to implement the MSE method is to enforce a constant depth and thickness for all frequencies in one measurement. This approach not only avoids fluctuations in the estimated parameters, it also significantly improves the processing speed of MSE. In this proposed approach, two MSE functions are defined instead of one. In the first MSE function (M_1), the dielectric property of the buried object (ε_{r3}) is estimated for different object depths (d_2 and d_4) and thicknesses (d_3):

$$M_1\left(d_2, d_3, d_4, f\right) = \min_{\varepsilon'_{r3}, \varepsilon''_{r3}} \left\{ M_0\left(d_2, d_3, d_4, \varepsilon'_{r3}, \varepsilon''_{r3}, f\right) \right\} \tag{3.12}$$

where M_1 is a 4-dimensional matrix of d_2, d_3, d_4 and f. M_1 has a minimized value for ε'_{r3} and ε''_{r3} at each frequency. In the second MSE function (M_2), by using the minimized M_1 in (3.12), object's depth and thickness are estimated,

$$M_2 = \min_{d_2, d_3, d_4} \left\{ \sum_{i=1}^{n} M_1\left(d_2, d_3, d_4, i\Delta f\right) \right\} \tag{3.13}$$

where M_2 has a minimized value for d_2, d_3 and d_4 after inspecting all the frequencies of interest. Using the estimated d_2, d_3 and d_4 in (3.13), the relative dielectric permittivity of the buried object (ε'_{r3} and ε''_{r3}) can be estimated by minimizing M_0 in (3.12). Implementing the proposed MSE provides two advantages over the existing methods [44, 72]. Firstly, fluctuations in the estimated ε_{r3} are reduced. Secondly, the processing speed is improved.

3.1.5 Analytical Path Loss Compensation

Ground penetrating radars operate close to the ground to improve signal-to-noise ratio (SNR) and to increase lateral resolution. Hence, the electromagnetic wave propagating onto the ground and to the buried object is mainly in the Fresnel region [48]. This method is unlike conventional free-space measurement methods, where electromagnetic plane wave in the far-field region is used to estimate the properties of materials [44, 73, 74]. The analysis in (3.7)−(3.10) in modeling multilayered dielectric slabs assumes the incident wave on the slabs (c.f. Fig. 3.1) is a plane wave. However, in UWB GPR, the incident wave is a spherical wave. If the calibration with the PEC sheet is performed on the surface of the object, the effect of spherical wave front for each case (PEC sheet calibration and object measurement) are identical and can be neutralized while deriving the ratio in (3.6). However, in practical problems, the PEC sheet, which is used for calibration, can only be placed on the surface of the ground, while the object is buried in the ground. This discrepancy will result in errors in estimating the buried object's properties if path loss due to the spherical wave is not accounted.

Calibration is the most commonly used method of accounting for the path loss [29]. However, an analytical method is proposed in this chapter. In the proposed method, dielectric permittivity of the material is estimated by comparing the reflection from PEC sheet and that from a slab at the same distance, d_1 (c.f. Fig. 3.4a). Hence, if the slab is at a different position from the PEC sheet, the reference plane of the PEC sheet needs to be translated to the new position before the physical and electrical properties of the buried object are estimated. Translation of the PEC reference can be done as follows: Let a source signal M be radiated by the Tx antenna aperture at $x = 0$ in Fig. 3.4a. At point Q, i.e. the location of the Rx antenna, scattered signal

from the PEC sheet is recorded. Since it is assumed the size of the PEC sheet is larger than the illumination area of the Tx antenna, the PEC sheet is assumed infinitely extended (c.f. Fig. 3.4a). Hence, image theory [48] can be applied to generate an image source (*M*') at $x = 2d_1$ (c.f. Fig. 3.4b).

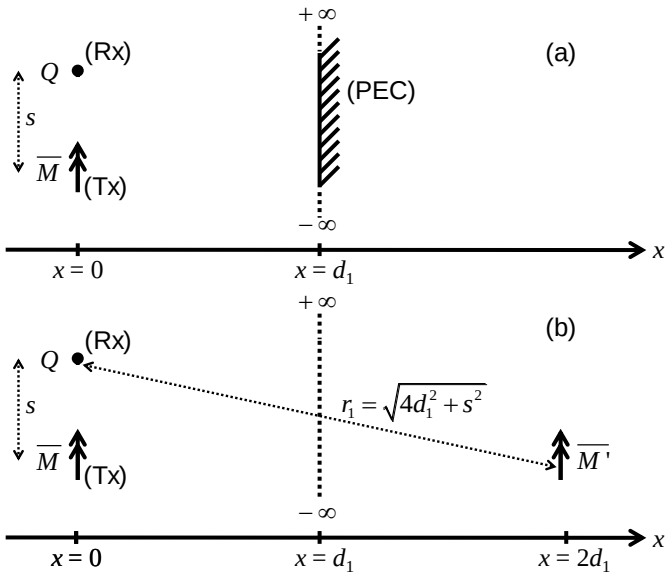

Fig. 3.4 Diagram showing the original problem (a) and its equivalent problem (b) by using image theory, in which a source (*M*) scattered by an infinitely extended perfect electrical conductor (PEC) is observed at point (*Q*).

The signal contribution by *M'*, observed at *Q*, can be derived using Friis transmission equation [48], in which the received signal power (P_{r1}) is related to the image source's signal power, P_t, as

$$P_{r1} = \left[\lambda/\left(4\pi r_1\right)\right]^2 G_t G_r P_t \tag{3.14}$$

where r_1 is the distance between *M'* and *Q*, $r_1^2 = 4d_1^2 + s^2$; G_t and G_r are the gain of the Tx and Rx antennas respectively, and λ is the free-space wavelength. If the PEC sheet is now placed at a different distance, for example, d_2, received power P_{r2} can be similarly derived using (3.14). Hence, the relationship between P_{r2} and P_{r1} can be derived as

$$P_{r2} = \left(r_1 / r_2\right)^2 P_{r1} \tag{3.15}$$

In terms of voltage, (3.15) can be re-written as

$$v_{r2}(t) = \left(r_1 / r_2\right) v_{r1}(t) \tag{3.16}$$

where $v_{r1}(t)$ and $v_{r2}(t)$ are the received signals due to the PEC sheet reflection at distances d_1 and d_2 respectively. To verify (3.16), received signals of an aluminium (assumed to be PEC) sheet placed at various distances (124 mm to 295 mm) from the UWB radar are recorded. The shape of the received signal shows consistency from 124 mm to 295 mm while the amplitude variations with respect to distance are compared with that of (3.16) in Fig. 3.5. It shows a good agreement between the proposed analytical model and measurement results.

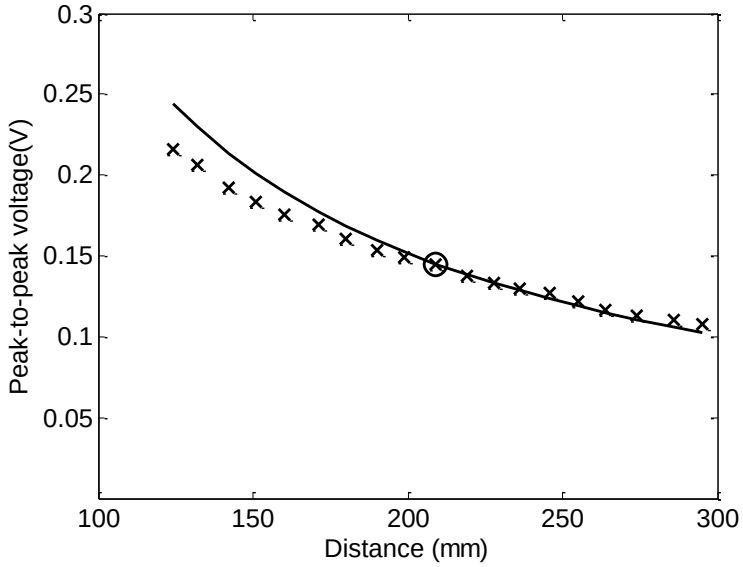

Fig. 3.5 Measured peak-to-peak voltages (Vpp) of the received signals from an aluminium sheet ('x') are compared with analytically modeled Vpp of received signal (solid line).

Although the analysis presented above is capable of predicting PEC sheet reflections at various distances in free-space, it does not account for wave refraction due to incident spherical waves on the ground as shown in Fig. 3.6.

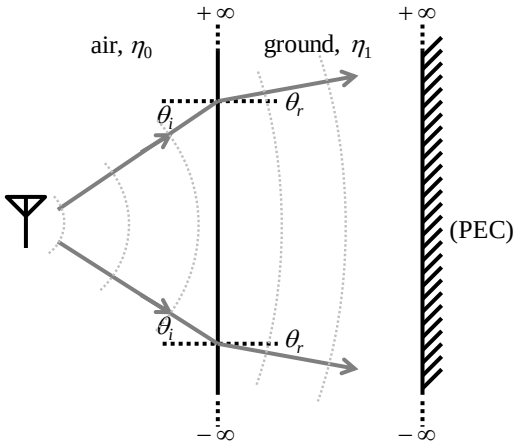

Fig. 3.6 Diagram showing the spherical wave refraction when it is incident on the air-to-ground discontinuity.

To estimate the path loss due to incident spherical waves on the ground, the PEC reflection on the ground surface needs to be translated to the interface between the ground and the buried object. By inspection (c.f. Fig. 3.6), we can compensate the effect of incident spherical wave refraction by incorporating the incident (θ_i) and refracted (θ_r) angles as the waves penetrate into the ground. In addition, by applying Snell's Law, (3.16) can be modified and simplified to

$$v_{rm}(t) = \left(d_g / d_m\right)^{\frac{\sin\theta_r}{\sin\theta_i}} v_{rg}(t) = \left(d_g / d_m\right)^{\frac{1}{\sqrt{\varepsilon_r}}} v_{rg}(t) \qquad (3.17)$$

where $v_{rg}(t)$ is the scattered signal when the PEC sheet is placed on the ground, and $v_{rm}(t)$ is the theoretical scattered signal when the PEC reference is in the ground after compensating for the path loss due to spherical waves. It should be emphasized that $v_{rm}(t)$ does not take into account of the scattering that occurs at the interface of air and the ground. It only accounts for the refraction effect when electromagnetic wave propagates into different material. d_g and d_m are the distance between the antennas and the front ground surface (interface 1−2 in Fig. 3.1), and the distance between the antennas and the front surface of the buried object (interface 2−3 in Fig. 3.1) respectively. Hence,

$$p(t)=\begin{cases} 1 & ,0\le t\le 2r_g/c \\ \left\{d_g/d_m(t)\right\}^{1/\sqrt{\varepsilon_r}} & ,t\ge 2r_g/c \end{cases} \tag{3.18}$$

where $p(t)$ is the path loss factor that needs to be multiplied with (3.6) to compensate for the path loss. $d_m(t)$ is defined as:

$$d_m(t)=d_g+\frac{c}{2\sqrt{\varepsilon_{rg}}}\left(t-\frac{2d_g}{c}\right) \tag{3.19}$$

Therefore, (3.6) can be rewritten as

$$\Gamma_{sc}(f)=-\frac{F\left\{\left[r_s(t)-r_a(t)\right]/\,p(t)\right\}}{F\left\{\left(r_m(t)-r_a(t)\right)\right\}} \tag{3.20}$$

where $\Gamma_{sc}(f)$ denotes the path loss compensated reflection coefficient of the ground with the buried object. The path loss factor $p(t)$ and the compensation effect on the received signal of the ground with buried object is shown in Fig. 3.7. It can be seen that compensation occurs after the reflection at the interface 1−2 in Fig. 3.1. The received signal is increasingly compensated if the reflections occur deeper in the ground.

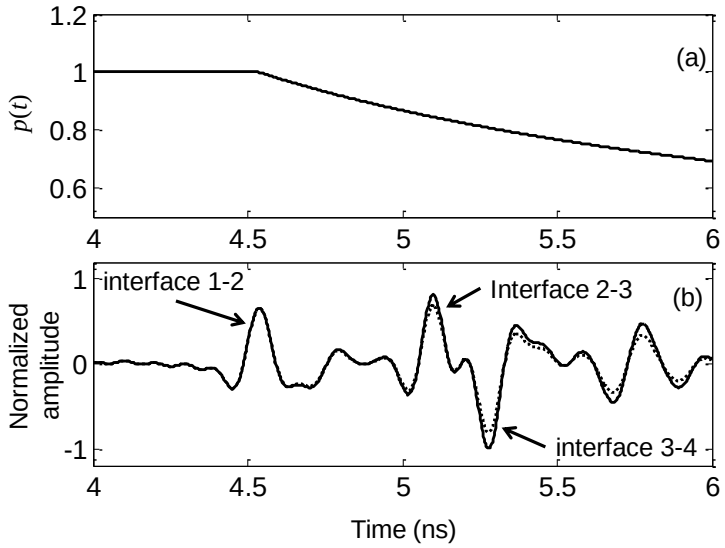

Fig. 3.7 Path loss compensation on the received signal. (a): path loss factor if ε_{rg} = 2.76. (b): Normalized received signal of the ground with buried object (dotted: without compensation, solid: with compensation)

3.2 Flowchart

The flowchart of the system employed in this work is shown in Fig. 3.8. As described in the flowchart, the received pulses are time aligned before being processed. The first time alignment accounts for the drift in the measurement system, while the second time alignment accounts for the thickness of the PEC sheet. Time gating is employed to remove undesired reflections in the received pulses. The numbers in brackets show the corresponding equations involved.

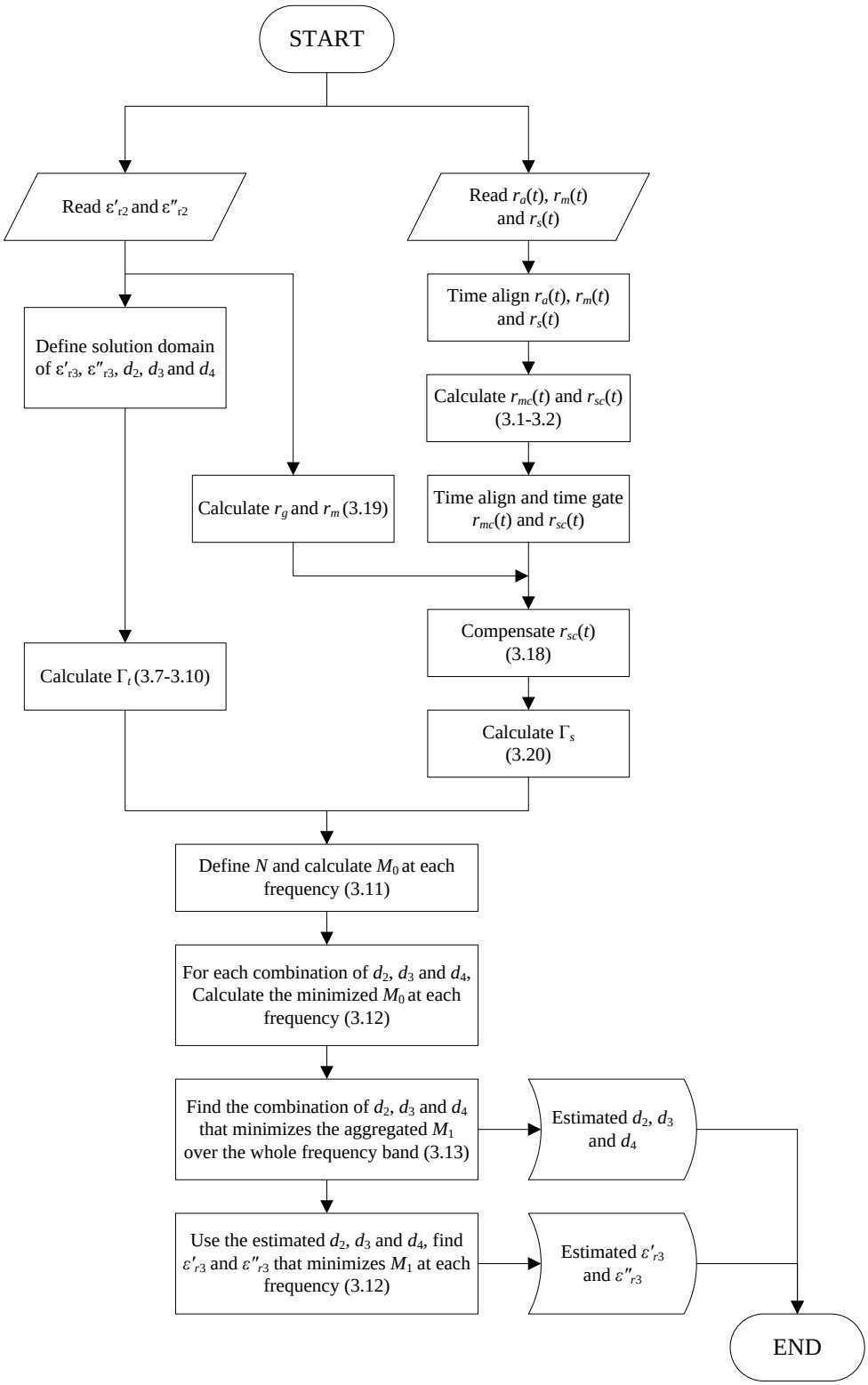

Fig. 3.8 The flowchart of the system

3.3 Measurement Procedure

Experiments are conducted to estimate the buried object physical and electrical properties using the proposed method. Fig. 3.9 and Fig. 3.10 describe the measurement setup. Sand is chosen as the ground material because it is the most commonly used material in the construction industry. As shown in Fig. 3.9, a rectangular slab is buried in sand which is contained by an open Styrofoam (ε_r = 1.03) box. The box is placed 350 mm above floor level to provide sufficient time interval between the desired reflections from the sand with the buried slab, and the undesired reflections from the floor. Time gating is used to effectively remove the undesired reflections in the received pulses.

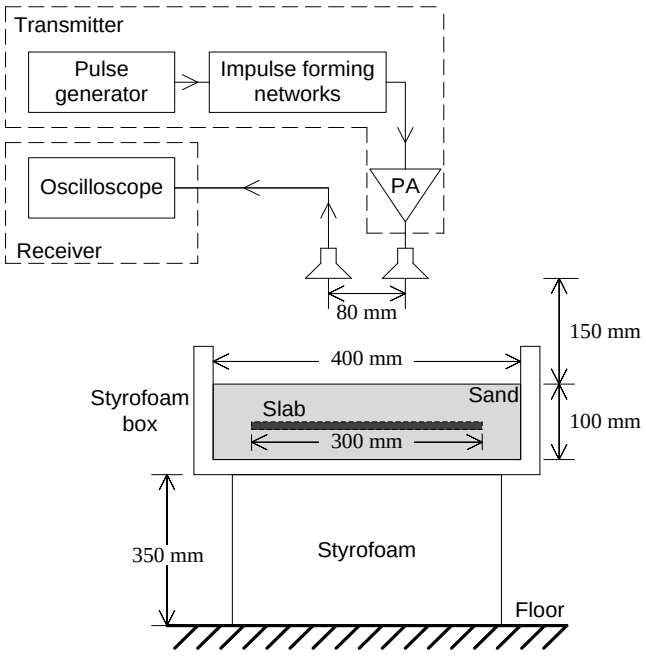

Fig. 3.9 Diagram describing the measurement setup to estimate the physical and electrical properties of buried objects.

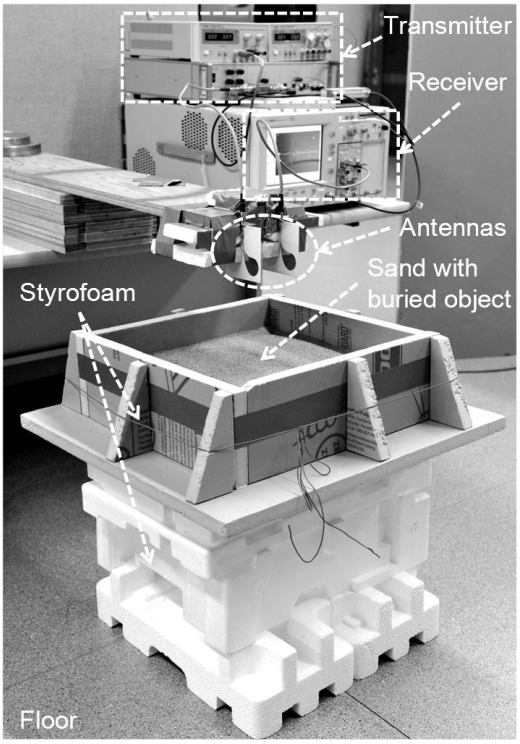

Fig. 3.10 Photo showing the measurement setup to estimate the physical and electrical properties of buried objects.

The UWB radar transmitter consists of a pulse generator, two impulse forming networks (IFNs) and a power amplifier (PA). The pulse generator (AVTECH AVP-3SA-C) generates a train of 10 V, 50 ps rise-time steps at 1 MHz pulse repetition frequency (PRF). Two IFNs (PSPL 5210) shape the generated pulse to a first derivative Gaussian pulse. The pulse/signal is amplified by a PA (Hittite HMC659LC5) to a peak-to-peak voltage of 5.454 V (Fig. 3.11). The wideband performance of the PA (17–19 dB @ DC–15GHz) ensures minimum distortion in the excitation pulse. The UWB radar receiver consists of a sampling oscilloscope (Agilent DCA 86100B) which samples the pulse at 40 GS/s. Time averaging is performed on the received pulses to improve the signal-to-noise ratio (SNR). As mentioned above, Vivaldi antennas are used as Tx and Rx antennas. The antennas

are placed side-by-side, at 80 mm apart, in a monostatic radar configuration. The distance between the antennas and the sand surface is 150 mm.

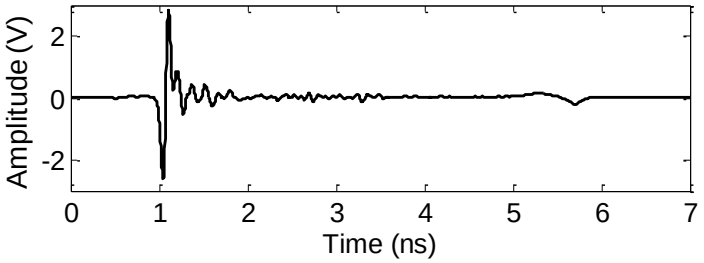

Fig. 3.11 Measured Gaussian monocycle pulse that is fed to the transmitting (Tx) antenna

The measurement procedure is as follows: First, $r_a(t)$ is recorded in free-space without the presence of the sand and the buried slab. Next, $r_m(t)$ is recorded when a large thin aluminium sheet (300×300 mm^2, $\sigma=3.56\times10^7$ S/m) is placed on top of the sand.

After calibration, $r_s(t)$ is recorded for the sand with the buried slab. An example of the measured pulses is shown in Fig. 3.12. Measured $r_a(t)$ shows some energy of the transmitted pulse is directly coupled to the receiving antenna at 3.8 ns (Fig. 3.12: 'A'). $r_a(t)$ also shows a visible reflection (Fig. 3.12: 'B') from the floor at 7.8 ns, verifying the height of the antennas from the floor is 0.6 m. Additional reflection from the aluminium sheet is visible in $r_m(t)$ at 4.6 ns (Fig. 3.12: 'C'). Furthermore, $r_s(t)$ shows the scattered pulses from the sand with the buried slab at 4.6 ns (Fig. 3.12: 'D'). $r_{mc}(t)$ and $r_{sc}(t)$ are the calibrated received pulses from the aluminium sheet, and sand with the buried object respectively. Notice that in these signals, antenna direct coupling has been removed. However, reflections from the floor are re-introduced in the procedure at 7.8 ns (Fig. 3.12: 'E'). These reflections can be eliminated by time-gating.

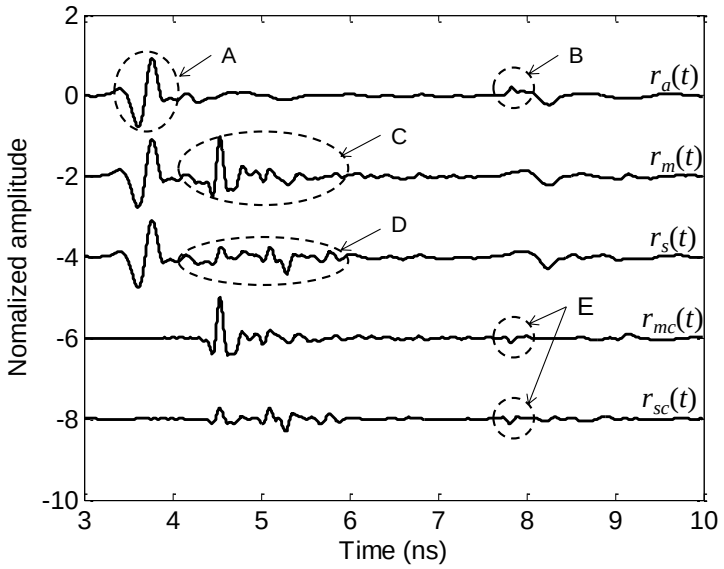

Fig. 3.12 Measured received pulses are plotted to illustrate the measurement and calibration process of the UWB radar.

Different construction materials are used to evaluate the performance of the UWB GPR. These materials are: Acrylic slab (disc-shaped with diameter of 685 mm and thickness of 23.76 mm), gypsum board (600×600×12.86 mm^3), marble tile (300×300×10.07mm^3), Formica laminate sheet (300×300×3.22 mm^3) and granite tile (300×300×10.34 mm^3). Only the marble tile, Formica laminate sheet and granite tile are buried in sand. The acrylic slab is too large in size, and the gypsum board has ε_r values that are very close to sand.

To verify the estimated objects' thicknesses, they are first measured with a vernier caliper. To validate the estimated ε_r values of the buried objects, their ε_r values are first measured in free-space. For free-space estimation, similar measurements and signal processing procedure are performed by restricting d_2 and d_4 to be zero. For further validation, estimated ε_r values of the buried objects are also compared with

measured ε_r values in the existing literature, and ε_r values measured with dielectric probe (Agilent 85070E).

3.4 Measurement Results

Measurements for sand, marble tile, Formica laminate sheet, granite tile, acrylic slab and gypsum board are performed to estimate their physical and electrical properties. In this section, results from these experiments are presented. The recovered electrical properties are described in terms of permittivity (ε'_r) and loss tangent ($\tan\delta$). A material's loss tangent is related to its complex dielectric permittivity as $\tan\delta = \varepsilon''_r / \varepsilon'_r$.

3.4.1 Sand

The relative permittivity (ε_r) of sand is measured before the measurements of buried objects. Sand layers of three different thicknesses are formed in the Styrofoam box for measurements. For each layer thickness, three measurements are conducted to estimate the sand's ε_r. Before each measurement, the sand surface is carefully re-leveled to minimize errors due to surface tilt and roughness. The effect of averaging on the estimated relative dielectric permittivity at 4.5 GHz (c.f. (3.11)) of a measurement is shown in Fig. 3.13. It can be seen from Fig. 3.13a that, without averaging (N=0), the estimated relative dielectric permittivity corresponding to minimum M_0 is 1.59 (dotted). For N=3 and 5, the estimated relative dielectric permittivity are 1.51 (dashed) and 2.65 (solid) respectively. This effect is shown more clearly in Fig. 3.13b. Without averaging, the estimated permittivity is lower in the frequency range of 4.4 GHz to 5.2 GHz. With averaging (N=5), the estimated value shows consistency in this frequency range (solid line). Consistency in the estimated dielectric permittivity values complies

with the fact that the permittivity changes gradually with respect to frequency. In the data process of all the measurements, we choose N=5.

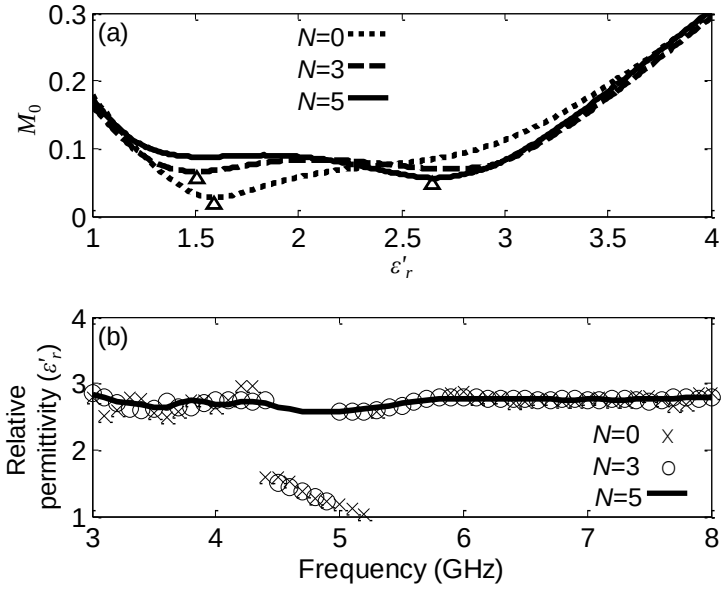

Fig. 3.13 Figure showing the effect of N on the estimated relative dielectric permittivity of sand. (a): M_0 of swept relative dielectric permittivity of sand at 4.5 GHz. (b): Estimated relative dielectric permittivity (ε'_r) of sand.

From multiple measurements on the same sand sample, it is observed that the estimated ε'_r values vary between 2.5 to 3.0 for different measurements (grey 'x' in Fig. 3.14a), with no observable trends for different sand thicknesses. Thus, it could be concluded that the ε'_r variations are due to imperfect leveling. The average estimated ε'_r and $\tan\delta$ values of sand are plotted as solid line in Fig. 3.14a and Fig. 3.14b respectively, showing ε'_r values are almost constant, and $\tan\delta$ values are negligibly small. Hence, the approximated electrical properties of sand are ε'_r = 2.76 and $\tan\delta$ = 0 in the frequency range of 3–8 GHz. The accuracy of estimated permittivity in the frequency range of 4.7 GHz to 4.9 GHz in some measurements could be further improved by increasing N. For comparison, as reported in [75], ε_r of beach sand was measured as 2.56–2.61 in the frequency range of 0.1−1.8 GHz.

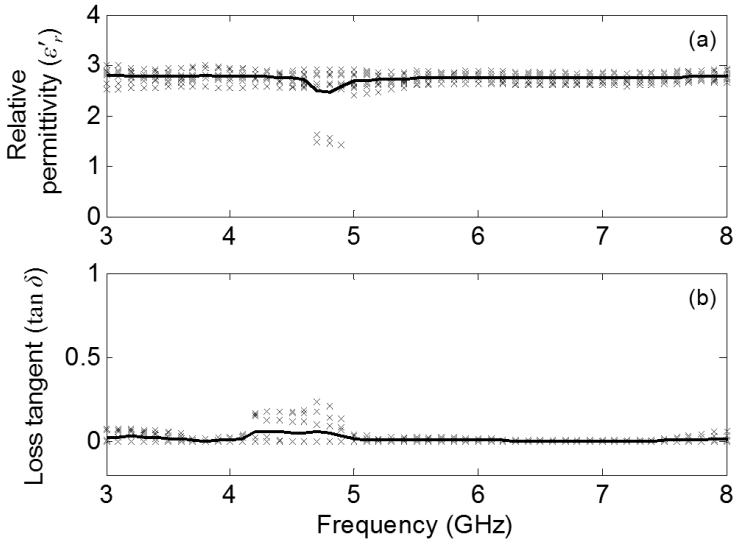

Fig. 3.14 Estimated relative dielectric permittivity (ε'_r) and loss tangent (tan δ) of sand are plotted in (a) and (b) respectively. Nine measurements, at various thicknesses, are conducted. Grey 'x' indicates estimated values in different measurements, while solid line indicates average values.

3.4.2 Marble

A marble tile is buried in the middle of a 100 mm thick sand layer. ε_r of the marble tile is estimated with the following steps: Using the measured received pulses and previously estimated ε_r of sand, $\Gamma_{sc}(f)$ in (3.20), is computed. Then, M_0, a 6-dimensional matrix, is formed. Applying the proposed two-stage mean square error (MSE) method, the physical and electrical properties of the buried marble tile are estimated. The optimized reflection coefficient is calculated using (3.10) and the estimated physical and electrical parameters. Fig. 3.15a and Fig. 3.15b compare the measured (solid line) and optimized ('x') reflection coefficients of the sand with the buried marble tile, showing a good agreement between them.

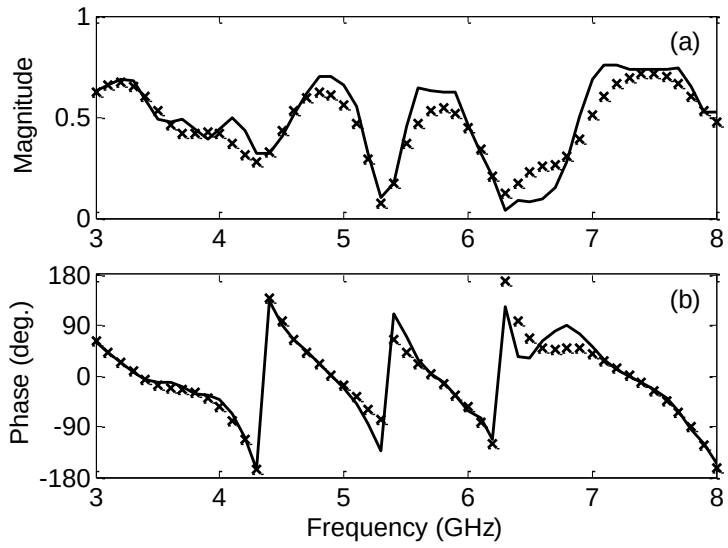

Fig. 3.15 Magnitude (a) and phase (b) of measured (solid line) and optimized ('x') reflection coefficient of sand with the buried marble slab are plotted and compared, showing a good agreement between them.

As shown in Fig. 3.16a, the estimated ε'_r of the buried marble tile is 8.0–9.8. These ε'_r values are comparable to [45], in which the estimated ε'_r of a dry Tennessee marble sample was reported to be 8.8 at 300 MHz and 8.6 at 10 GHz. The result of the dielectric probe measurement is also shown in grey solid line in the same figure for comparison. The estimated thickness is 9.0 mm, which is comparable to 10.07 mm when measured with a vernier caliper. To illustrate the improvement of the proposed path loss compensation method, the estimated ε'_r and $\tan\delta$ of the buried marble tile are plotted with (dashed line) and without (dotted line) path loss compensation in Fig. 3.16a and Fig. 3.16b. These two sets of data are compared with the estimated ε'_r and $\tan\delta$ of the marble tile in free-space (solid line, Fig. 3.16a and Fig. 3.16b). Visual inspection of Fig. 3.16a and Fig. 3.16b indicates the path loss compensation significantly improves the accuracy of the estimated ε'_r and $\tan\delta$. Numerically, the average value of marble's ε'_r and $\tan\delta$ are 9.29 and 0.01 in free-space respectively. When the marble tile is buried in sand, without path loss

compensation, it's estimated ε'_r and $\tan\delta$ are 8.19 and 0.08. However, with path loss compensation, it's estimated ε'_r and $\tan\delta$ are 9.00 and 0.002.

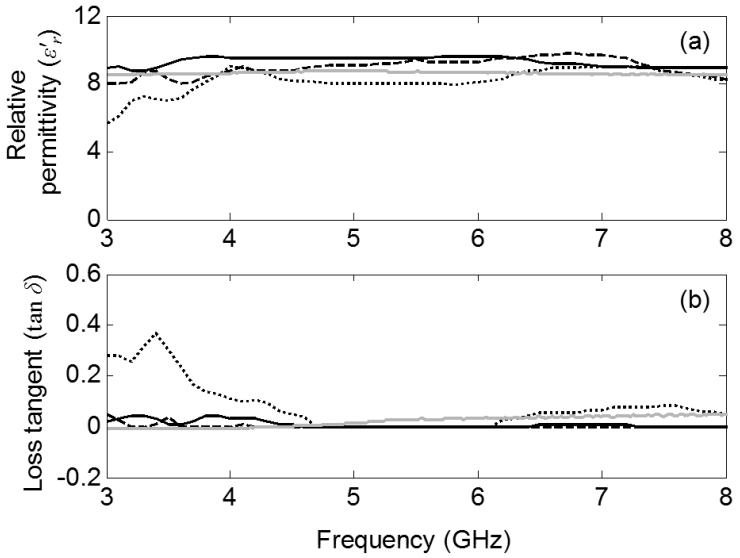

Fig. 3.16 Estimated relative dielectric permittivity (ε'_r) and loss tangent (tan δ) of marble tile are plotted in (a) and (b) respectively. Estimation based on free-space measurement is plotted as black solid line. The measured result with dielectric probe is shown in grey solid line. Estimations of the buried marble tile with and without path loss compensation, are plotted as dashed and dotted lines respectively.

3.4.3 Formica Laminate Sheet

A thin Formica laminate sheet is buried in the middle of a 100 mm thick sand layer. As shown in Fig. 3.17a, the estimated ε'_r of the buried laminate sheet is 5.5–7.1. The author is unable to find any reported dielectric measurement result of the same material. However, in [45], a field parallel Formica laminate was reported to have an ε'_r of 4.5 at low frequencies (< 1 MHz), and about 3.4 at 10 GHz. The result of the dielectric probe measurement is plotted as grey solid line in Fig. 3.17 for comparison. The estimated thickness is 2.7 mm, which is comparable to 3.22 mm when measured with a vernier caliper.

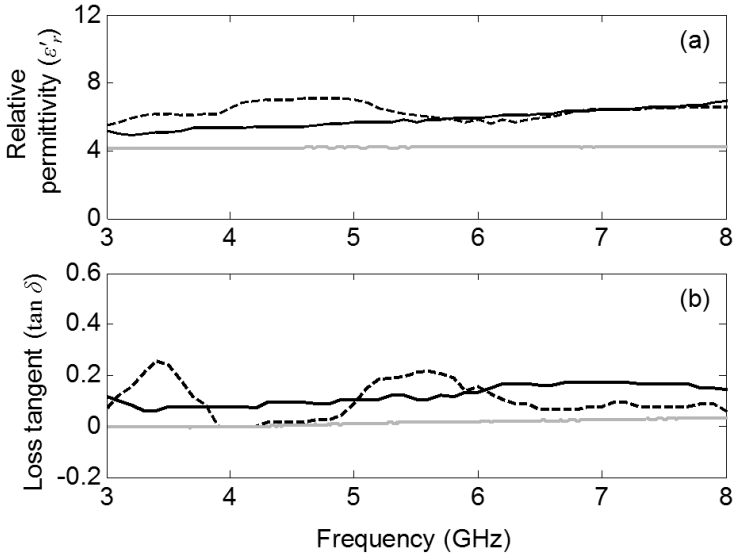

Fig. 3.17 Estimated relative dielectric permittivity (ε'_r) and loss tangent (tan δ) of Formica laminate sheet are plotted in (a) and (b) respectively. Estimation based on free-space measurement is plotted as black solid line, and estimations of the buried Formica laminate sheet with path loss compensation is plotted as dashed line. The measured result with dielectric probe is shown in grey solid line.

3.4.4 Granite

A granite tile is buried in the middle of a 100 mm thick sand layer. As shown in Fig. 3.18a, the estimated ε'_r of the buried granite tile is 7.1−11.9. These values are comparable to the reported values in [76], which estimated the ε'_r of a dry granite sample to be 7.0 at 100 MHz. The measured relative dielectric permittivity with the dielectric probe is shown in grey solid line in the same figure for comparison. The estimated thickness is 10.0 mm, which is comparable to vernier caliper measurement of 10.34 mm.

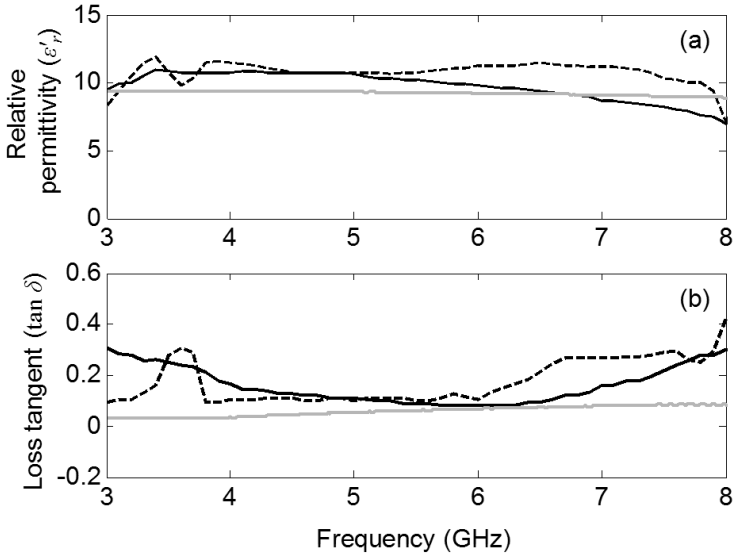

Fig. 3.18 Estimated relative dielectric permittivity (ε'_r) and loss tangent (tan δ) of granite tile are plotted in (a) and (b) respectively. Estimation based on free-space measurement is plotted as black solid line, and estimations of the buried granite tile with path loss compensation is plotted as dashed line. The measured result with the dielectric probe is shown in grey solid line.

3.4.5 Acrylic and Gypsum

Acrylic slab and gypsum board are measured in free-space. The estimated ε'_r of acrylic slab (Fig. 3.19a) is 2.7 − 3.0. This is comparable to [77], where it was reported that the measured ε'_r value was between 2.48–2.51 in the frequency range of 2–18 GHz. The estimated ε'_r of gypsum board (Fig. 3.19a) is between 1.59–2.27. These values are validated by [78], where measured ε'_r values of 2.41–2.60 were reported in the frequency range of 0–6 GHz. The measured result of the gypsum board with the dielectric probe is shown in grey solid line. The dielectric probe measurement of the acrylic slab was not performed because the sample was not available at the moment of measurement.

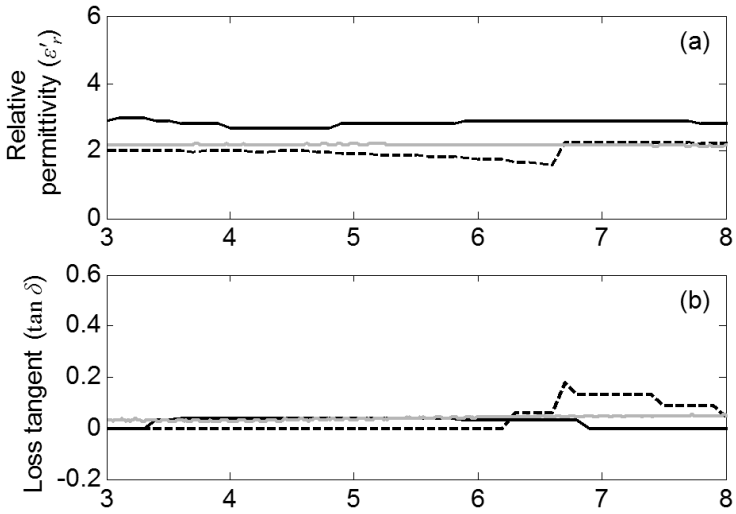

Fig. 3.19 Estimated relative dielectric permittivity (ε'_r) and loss tangent (tan δ) of acrylic slab (solid line) and gypsum board (dashed line) are plotted in (a) and (b) respectively. The dielectric probe measurement result of the gypsum board is shown in grey solid line.

It can be seen from the above measurement results that the estimated dielectric properties of the buried objects with the proposed method show good agreement with those measured with the dielectric probe. The dielectric probe measurement result of the Formica laminate sheet may not be valid since the thickness of the Formica laminate sheet does not satisfy the requirement of dielectric probe measurement. The minimum thickness of the Formica laminate sheet of dielectric probe measurement has to be at least 10 mm [79]. The inhomogeneity in the dielectric permittivity profile of the granite tile is detected when it is measured with the dielectric probe. It should be noted that the accuracy of this method will be lower in estimating high lossy objects. The reason is the signal-to-noise (SNR) ratio of the reflection, from the bottom surface of the object, is low due to the loss in the object.

Comparison between the estimated and vernier caliper measured thicknesses is shown in TABLE 3.1.

TABLE 3.1 TABLE COMPARING OBJECT THICKNESS MEASURED WITH DIFFERENT METHODS (VERNIER CALIPER, FREE-SPACE AND BURIED IN SAND)

Object	Measured Thickness (mm)		
	Vernier Caliper	Free-Space	Buried in Sand
Marble tile	10.07	9.5	9.0
Laminate sheet	3.22	3.7	2.7
Granite tile	10.34	10.0	9.7
Acrylic slab	23.76	22.0	–
Gypsum board	12.86	13.0	–

TABLE 3.1 summarizes the estimated thicknesses of all the objects using the proposed radar method and compares them with those of vernier caliper. The comparisons show the proposed method can achieve an average accuracy of ± 0.7 mm. Both the estimated physical and electrical properties of the buried objects show that the proposed method is capable of achieving sufficient accuracy in estimating the ε_r of buried objects for the purpose of object material identification. Accuracy of the estimated object thickness is dependent on the width of the excitation pulse, as well as the electrical properties of the object. Probing depth of the UWB GPR is dependent on the power of the excitation pulse, the receiver sensitivity, and the electrical properties of the ground material and the buried object. For an excitation pulse of 1W peak power and soil relative permittivity of 4, when the received pulse is averaged 5000 times, the proposed UWB GPR can detect a metal planar object at 1m depth.

3.5 Summary

In this chapter, we have demonstrated the capability of the UWB radar in characterizing objects that are buried in the ground. In the proposed method, the received time-domain signals of the radar are processed to estimate the depth, thickness and frequency dependent permittivity profiles of the buried object. In the parameter optimization process, a constant object depth and thickness is enforced at all frequencies, resulting in a more accurate estimation of buried objects' characteristics and a reduced processing time. In addition, path loss due to the close proximity of the UWB radar to the ground has been compensated analytically.[2]

[2] *A version of this chapter has been submitted for publication in IEEE Transactions on Microwave Theory and Techniques.*

Chapter-IV

4 Conclusion

4.1 Discussion

The study of scattered UWB pulses has significant importance for various applications such as diagnosis of breast cancer [8-10], detecting and localizing moving targets [13] and military stealth designs [19, 20]. UWB technology is also extensively used in ground penetrating radars (GPRs) [21] to locate buried pipes [27], investigate concrete structures [28] and check the integrity of pavements [30]. This thesis described studies addressing two problems in UWB technology.

In the first study, we proposed a method of estimating the characteristics of UWB pulse scattered from metal planar objects in the far-field. When the object is in the near-field, the transition of the scattered pulse shape is studied. We also studied the effect of multiple scattering on the shape and amplitude of the scattered pulse. Furthermore, we defined a frequency-averaged radar cross section (RCS) of the metal planar object. We found excellent agreement between the estimated and measured scattered pulses for metal planar objects with dimensions of 100 X 100 mm^2, 160 X 160 mm^2 and 200 X 200 mm^2. For the same objects, the estimated frequency-averaged RCS are close to narrowband conventional RCS [59].

In the second study, we proposed a method of characterizing buried objects in the ground using UWB GPR. In this method, UWB pulses are radiated by the radar, while scattered pulses from the ground with the buried object are received. The received pulses are then post-processed to estimate the depth, thickness and

electrical properties of the buried object. A constant depth and thickness are enforced at all frequencies while the signals are processed to extract the buried object characteristics, resulting in more accurate estimations and reduced processing time. Moreover, path loss due to the close proximity of the radar to the ground is compensated analytically.

4.2 Future work

The proposed method of computing the shape and energy of the UWB pulse scattered from metal planar objects can be extended to the analysis of metallic objects of different shapes. This will simplify the procedure of estimating the coverage area of UWB radars, allowing radar engineers to analytically estimate the transmitted pulse and optimize the transmit power in radar systems.

In the analysis of UWB pulse scattered from buried dielectric slabs, multiple transmitting (Tx) and receiving (Rx) antenna pairs can be arranged to form an antenna array configuration to provide a three-dimensional (3D) profile of the buried objects. The UWB GPR system can be prototyped with low cost components such as direct digital synthesizers (DDSs), step-recovery diodes (SRDs), power amplifiers (PAs), mixers, low noise amplifiers (LNAs), analog-to-digital converters (ADCs) and a single chip microcomputer (SCM). Time expansion method [80] can be used to sample the scattered UWB pulse from the objects to alleviate the requirement of the speed of the ADC. Furthermore, the UWB radar technology can be incorporated into the existing tunnel boring machines (TBMs). In this application, practical issues such as moisture content in the soil, harsh construction environment and a large probing area have to be taken into account. To maintain a required probing depth in tunnels with different

moisture content, the number of received pulses in the averaging of the receiver can be changed accordingly. Multiple UWB GPR units can be mounted on the rotating platform of the TBM to scan the tunnel face. Radomes can be used to cover the UWB GPR units to protect the Tx and Rx antennas while probing the tunnel. Successful incorporation of the UWB GPRs into the existing TBMs provides valuable fore-knowledge of the buried geological features in front of the TBM, giving the operator opportunity to react to any perceived dangers during tunnel construction.

References

[1] K. Siwiak and D. McKeown, *Ultra-wideband radio technology*. England: John Wiley and Sons, Ltd., 2004.

[2] R. A. Scholtz, R. Weaver, E. Homier, J. Lee, P. Hilmes, A. Taha, and R. Wilson, "UWB radio deployment challenges," in *Personal, Indoor and Mobile Radio Communications, 2000. PIMRC 2000. The 11th IEEE International Symposium on*, 2000, pp. 620-625 vol.1.

[3] D. Cassioli, M. Z. Win, F. Vatalaro, and A. F. Molisch, "Performance of low-complexity RAKE reception in a realistic UWB channel," in *Communications, 2002. ICC 2002. IEEE International Conference on*, 2002, pp. 763-767 vol.2.

[4] S. S. Kolenchery, J. K. Townsend, and J. A. Freebersyser, "A novel impulse radio network for tactical military wireless communications," in *Military Communications Conference, 1998. MILCOM 98. Proceedings., IEEE*, 1998, pp. 59-65 vol.1.

[5] P. S. Kildal, A. A. Kishk, and A. Tengs, "Reduction of forward scattering from cylindrical objects using hard surfaces," *Antennas and Propagation, IEEE Transactions on*, vol. 44, pp. 1509-1520, 1996.

[6] H. Thielen, "Reduction of the strut radiation of reflector antennas," in *Antennas and Propagation Society International Symposium, 1981*, 1981, pp. 504-507.

[7] P.-S. Kildal, "Artificially soft and hard surfaces in electromagnetics and their application to antenna design," in *Microwave Conference, 1993. 23rd European*, 1993, pp. 30-33.

[8] S. M. Salvador and G. Vecchi, "Experimental Tests of Microwave Breast Cancer Detection on Phantoms," *Antennas and Propagation, IEEE Transactions on*, vol. 57, pp. 1705-1712, 2009.

[9] S. Takaichi, A. Mase, K. Yuichiro, H. Hojo, and K. Kang Wook, "Simulation study and experiment of breast cancer detection using an ultrashort-pulse radar," in *Microwave Conference, 2008. APMC 2008. Asia-Pacific*, 2008, pp. 1-4.

[10] Y. Chen, E. Gunawan, Y. Kim, K. S. Low, C. B. Soh, and L. L. Thi, "UWB Microwave Breast Cancer Detection: Generalized Models and Performance Prediction," in *Engineering in Medicine and Biology Society, 2006. EMBS '06. 28th Annual International Conference of the IEEE*, 2006, pp. 2630-2633.

[11] M. Dehmollaian and K. Sarabandi, "An Approximate Solution of Scattering From Reinforced Concrete Walls," *Antennas and Propagation, IEEE Transactions on*, vol. 56, pp. 2681-2690, 2008.

[12] R. Paknys, "Reflection and transmission by reinforced concrete - numerical and asymptotic analysis," *Antennas and Propagation, IEEE Transactions on*, vol. 51, pp. 2852-2861, 2003.

[13] W. Guohua, Z. Yuxiang, and W. Siliang, "Detection and localization of high speed moving targets using a short-range UWB impulse radar," in *Radar Conference, 2008. RADAR '08. IEEE*, 2008, pp. 1-4.

[14] R. G. Madonna, P. J. Scheno, and J. Scannapieco, "Diffraction of ultrawide band radar pulses," *Proc. SPIE 1631, 165 (1992)*.

[15] D. Weissman and T. Thompson, "Detection and interpretation of ocean roughness variations across the gulf stream inferred from radar cross section observations," in *OCEANS '77 Conference Record*, 1977, pp. 161-170.

[16] F. Feindt, V. Wismann, W. Alpers, and W. C. Keller, "Airborne measurements of the ocean radar cross section at 5.3 GHz as a function of wind speed," *Radio Sci., 21(5), 845–856*, 1986.

[17] V. Hesany, W. J. Plant, and W. C. Keller, "The normalized radar cross section of the sea at 10° incidence," *Geoscience and Remote Sensing, IEEE Transactions on*, vol. 38, pp. 64-72, 2000.

[18] K. Iwaszczuk, H. Heiselberg, and P. U. Jepsen, "Terahertz radar cross section measurements," in *Infrared Millimeter and Terahertz Waves (IRMMW-THz), 2010 35th International Conference on*, 2010, pp. 1-3.

[19] P. Bidigare, T. Stevens, B. Correll, and M. Beauvais, "Minimum radar cross section bounds for passive radar responsive tags," in *Signals, Systems and Computers, 2004. Conference Record of the Thirty-Eighth Asilomar Conference on*, 2004, pp. 1441-1445 Vol.2.

[20] R. K. Dutta, "Theoretical determination of monostatic co- & cross-linearly polarized radar cross section of a missile at each point of missile trajectory - Part II: Simulation results," in *Recent Advances in Microwave Theory and Applications, 2008. MICROWAVE 2008. International Conference on*, 2008, pp. 930-933.

[21] C. C. Chen, J. T. Johnson, M. Sato, and A. G. Yarovoy, "Foreword to the Special Issue on Subsurface Sensing Using Ground-Penetrating Radar (GPR)," *Geoscience and Remote Sensing, IEEE Transactions on*, vol. 45, pp. 2419-2421, 2007.

[22] J. Francke, "Applications of GPR in mineral resource evaluations," in *Ground Penetrating Radar (GPR), 2010 13th International Conference on*, 2010, pp. 1-5.

[23] W. I. Linlor and G. R. Jiracek, "Electromagnetic reflection from multi-layered snow models," *Journal of Glaciology,* vol. 14, pp. 501-515, 1975.

[24] G. Grazzini, M. Pieraccini, F. Parrini, A. Spinetti, G. Macaluso, D. Dei, and C. Atzeni, "An ultra-wideband high-dynamic range GPR for detecting buried people after collapse of buildings," in *Ground Penetrating Radar (GPR), 2010 13th International Conference on*, 2010, pp. 1-6.

[25] E. Utsi, "The shrine of edward the confessor: A study in multi-frequency gpr investigation," in *Ground Penetrating Radar (GPR), 2010 13th International Conference on*, 2010, pp. 1-7.

[26] K. O'Neill, S. A. Haider, S. D. Geimer, and K. D. Paulsen, "Effects of the ground surface on polarimetric features of broadband radar scattering from subsurface metallic objects," *Geoscience and Remote Sensing, IEEE Transactions on,* vol. 39, pp. 1556-1565, 2001.

[27] G. Borgioli, L. Capineri, P. L. Falorni, S. Matucci, and C. G. Windsor, "The Detection of Buried Pipes From Time-of-Flight Radar Data," *Geoscience and Remote Sensing, IEEE Transactions on,* vol. 46, pp. 2254-2266, 2008.

[28] T. Roackaway and J. A. Rivard, "Application of ground penetrating radar in the urban environment," in *Ground Penetrating Radar (GPR), 2010 13th International Conference on*, 2010, pp. 1-4.

[29] U. Spagnolini, "Permittivity measurements of multilayered media with monostatic pulse radar," *Geoscience and Remote Sensing, IEEE Transactions on,* vol. 35, pp. 454-463, 1997.

[30] K. Umashankar and A. Taflove, "A Novel Method to Analyze Electromagnetic Scattering of Complex Objects," *Electromagnetic Compatibility, IEEE Transactions on,* vol. EMC-24, pp. 397-405, 1982.

[31] X. Wang, Y. Lu, and X. Yu, "Electromagnetic wave scattering on irregular metal column or irregular metal surface (TE-case)," in *Computational Electromagnetics and Its Applications, 1999. Proceedings. (ICCEA '99) 1999 International Conference on*, 1999, pp. 460-463.

[32] S. Harma and V. P. Plessky, "Extraction of frequency-dependent reflection, transmission, and scattering parameters for short metal reflectors from FEM-BEM simulations," *Ultrasonics, Ferroelectrics and Frequency Control, IEEE Transactions on,* vol. 55, pp. 883-889, 2008.

[33] F. Horner, "Scattering of radio waves by metal wires and sheets," *Proceedings of the IEE - Part III: Radio and Communication Engineering,* vol. 96, pp. 333-340, 1949.

[34] M. Herberthson, "Application of the potential method for determining the radar cross section of electrically large objects," in *General Assembly and Scientific Symposium, 2011 XXXth URSI*, 2011, pp. 1-4.

[35] M. E. Bechtel, "Application of geometric diffraction theory to scattering from cones and disks," *Proceedings of the IEEE,* vol. 53, pp. 877-882, 1965.

[36] X. Fang and D. Su, "Prediction of in-flight aircraft radar cross-section," in *Antennas, Propagation and EM Theory, 2008. ISAPE 2008. 8th International Symposium on*, 2008, pp. 526-529.

[37] D. Colak, A. I. Nosich, and A. Altintas, "Radar cross-section study of cylindrical cavity-backed apertures with outer or inner material coating: the case of H-polarization," *Antennas and Propagation, IEEE Transactions on,* vol. 43, pp. 440-447, 1995.

[38] C. C. Courtney, "Time-domain measurement of the electromagnetic properties of materials," *Microwave Theory and Techniques, IEEE Transactions on,* vol. 46, pp. 517-522, 1998.

[39] S. Bakhtiari, N. Qaddoumi, S. I. Ganchev, and R. Zoughi, "Microwave noncontact examination of disbond and thickness variation in stratified composite media," *Microwave Theory and Techniques, IEEE Transactions on,* vol. 42, pp. 389-395, 1994.

[40] A. M. Paz, S. Trabelsi, S. O. Nelson, and E. Thorin, "Measurement of the Dielectric Properties of Sawdust Between 0.5 and 15 GHz," *Instrumentation and Measurement, IEEE Transactions on,* vol. 60, pp. 3384-3390, 2011.

[41] A. M. Nicolson and G. F. Ross, "Measurement of the Intrinsic Properties of Materials by Time-Domain Techniques," *Instrumentation and Measurement, IEEE Transactions on,* vol. 19, pp. 377-382, 1970.

[42] D. L. Faircloth, M. E. Baginski, and S. M. Wentworth, "Complex permittivity and permeability extraction for multilayered samples using S-parameter waveguide measurements," *Microwave Theory and Techniques, IEEE Transactions on,* vol. 54, pp. 1201-1209, 2006.

[43] O. M. Bucci, G. Cortucci, G. Franceschetti, C. Savarese, and R. Tiberie, "Time-Domain Techniques for Measuring the Conductivity and Permittivity Spectrum of Materials," *Instrumentation and Measurement, IEEE Transactions on,* vol. 21, pp. 237-243, 1972.

[44] D. K. Ghodgaonkar, V. V. Varadan, and V. K. Varadan, "A free-space method for measurement of dielectric constants and loss tangents at microwave frequencies," *Instrumentation and Measurement, IEEE Transactions on,* vol. 38, pp. 789-793, 1989.

[45] A. R. v. Hippel, *Dielectric materials and applications*. New York: MIT Technology Press, 1954.

[46] M. N. Afsar, J. R. Birch, R. N. Clarke, and G. W. Chantry, "The measurement of the properties of materials," *Proceedings of the IEEE,* vol. 74, pp. 183-199, 1986.

[47] P. Chaturvedi and R. G. Plumb, "Electromagnetic imaging of underground targets using constrained optimization," *Geoscience and Remote Sensing, IEEE Transactions on,* vol. 33, pp. 551-561, 1995.

[48] C. A. Balanis, *Antenna Theory Analysis and Design*, 3rd ed. New York: Wiley, 2005.

[49] M. Nakhkash, H. Yi, and M. T. C. Fang, "Application of the multilevel single-linkage method to one-dimensional electromagnetic inverse scattering problem," *Antennas and Propagation, IEEE Transactions on,* vol. 47, pp. 1658-1668, 1999.

[50] M. E. Requena-Perez, A. Albero-Ortiz, J. Monzo-Cabrera, and A. Diaz-Morcillo, "Combined use of genetic algorithms and gradient descent optmization methods for accurate inverse permittivity measurement," *Microwave Theory and Techniques, IEEE Transactions on,* vol. 54, pp. 615-624, 2006.

[51] M. Santra and K. U. Limaye, "Estimation of complex permittivity of arbitrary shape and size dielectric samples using cavity measurement technique at microwave frequencies," *Microwave Theory and Techniques, IEEE Transactions on,* vol. 53, pp. 718-722, 2005.

[52] T. Zwick, J. Haala, and W. Wiesbeck, "A genetic algorithm for the evaluation of material parameters of compound multilayered structures," *Microwave Theory and Techniques, IEEE Transactions on,* vol. 50, pp. 1180-1187, 2002.

[53] A. Elhawil, G. Koers, L. Zhang, J. Stiens, and R. Vounckx, "Comparison between two optimisation algorithms to compute the complex permittivity of dielectric multilayer structures using a free-space quasi-optical method in W-band," *Science, Measurement & Technology, IET,* vol. 3, pp. 13-21, 2009.

[54] H. W. Lorber, "A time domain radar range equation," in *Ultrawideband, Short-Pulse Electromagnetics*, L. Carin and L. B. Felsen, Eds., ed New York: Plenum, 1995.

[55] K. A. Shubert and G. T. Ruck, "Canonical representation of the radar range equation in the time domain," *Proc. SPIE 1631, 2 (1992).*

[56] A. Shlivinski, E. Heyman, and R. Kastner, "Antenna characterization in the time domain," *Antennas and Propagation, IEEE Transactions on,* vol. 45, pp. 1140-1149, 1997.

[57] C. Harrison, Jr. and C. Williams, Jr., "Transients in wide-angle conical antennas," *Antennas and Propagation, IEEE Transactions on,* vol. 13, pp. 236-246, 1965.

[58] W. A. v. Cappellen, "Ultra-short pulse time domain radar cross section measurements," Master Thesis, Delft University of Technology, Delft, Netherlands, 1998.

[59] E. F. Knott, "Radar Cross Section," in *Radar Handbook*, I. Skolnik, Ed., 3rd ed New York: McGraw-Hill, 2008.

[60] C. A. Balanis, *Advanced Engineering Electromagnetics*. New York: Wiley, 1989.

[61] B. R. Mayo, P. W. Howells, and W. B. Adams, "Generalized linear radar analysis," *Microwave J., vol. 3, p.79 , 1961*.

[62] M. Kanda, "Transients in a resistively loaded linear antenna compared with those in a conical antenna and a TEM horn," *Antennas and Propagation, IEEE Transactions on,* vol. 28, pp. 132-136, 1980.

[63] K. Rambabu, A. E. C. Tan, K. K. M. Chan, and M. Y. W. Chia, "Estimation of Antenna Effect on Ultra-Wideband Pulse Shape in Transmission and Reception," *Electromagnetic Compatibility, IEEE Transactions on,* vol. 51, pp. 604-610, 2009.

[64] X. Qing, Z. N. Chen, and a. M. Y. W. Chia, "Characterization of ultrawideband antennas using transfer functions," *Radio Sci., 41, RS1002,* 2006.

[65] S. Sczyslo, H. Thye, G. Armbrecht, S. Dortmund, and T. Kaiser, "Determination of the impulse response of UWB antennas using GTEM cells," in *Ultra-Wideband, 2009. ICUWB 2009. IEEE International Conference on*, 2009, pp. 753-758.

[66] X. M. Qing and Z. N. Chen, "Antipodal Vivaldi antenna for UWB applications," in *Proc. Euro Electromag.-UWB SP7*, Magdeburg, Germany, July 12-16, 2004.

[67] G. Quintero, J. F. Zurcher, and A. K. Skrivervik, "System Fidelity Factor: A New Method for Comparing UWB Antennas," *Antennas and Propagation, IEEE Transactions on,* vol. 59, pp. 2502-2512, 2011.

[68] K. Rambabu, A. E. C. Tan, K. K. M. Chan, and M. Y. W. Chia, "Experimental Verification of Link Loss Analysis for Ultrawideband Systems," *Antennas and Propagation, IEEE Transactions on,* vol. 59, pp. 1428-1432, 2011.

[69] J. R. Andrews, "UWB Signal Sources, Antenna & Propagation," Picosecond Pulse lab, Application Notes: AN-14a Aug. 2003.

[70] A. E. C. Tan and M. Y. W. Chia, "Measuring human body impulse response using UWB radar," *Electronics Letters,* vol. 41, pp. 1193-1194, 2005.

[71] S. Ramo, J. R. Whinnery, and T. V. Duzer, *Fields and Waves in Communication Electronics*, 3rd ed.: John Wiley, 1994, ch6.

[72] F. Sagnard and G. E. Zein, "In situ characterization of building materials for propagation modeling: frequency and time responses," *Antennas and Propagation, IEEE Transactions on,* vol. 53, pp. 3166-3173, 2005.

[73] F. A. M. Zaki, Z. Awang, N. H. Baba, A. S. Zoolfakar, R. A. Bakar, M. Zolkapli, and N. Fadzlina, "A free-space method for measurement of complex permittivity of double-layer dielectric materials at microwave frequencies," in *Research and Development (SCOReD), 2010 IEEE Student Conference on*, 2010, pp. 12-15.

[74] R. Grignon, M. N. Afsar, W. Yong, and S. Butt, "Microwave broadband free-space complex dielectric permittivity measurements on low loss solids," in *Instrumentation and Measurement Technology Conference, 2003. IMTC '03. Proceedings of the 20th IEEE*, 2003, pp. 865-870.

[75] C. Matzler, "Microwave permittivity of dry sand," *Geoscience and Remote Sensing, IEEE Transactions on,* vol. 36, pp. 317-319, 1998.

[76] M. S. Amant, "Frequency and temperature dependence of dielectric properties of some common rocks," MSc Dissertation, Massachusetts Institute of Technology, Cambridge, MA, Appendix B, 1968.

[77] E. J. Rothwell, "Extraction of the Wideband Dielectric Properties of a Material Layer Using Measured Natural Frequencies," *Antennas and Propagation, IEEE Transactions on,* vol. 58, pp. 620-623, 2010.

[78] C. A. Grosvenor, R. T. Johnk, J. Baker-Jarvis, M. D. Janezic, and B. Riddle, "Time-Domain Free-Field Measurements of the Relative Permittivity of Building Materials," *Instrumentation and Measurement, IEEE Transactions on,* vol. 58, pp. 2275-2282, 2009.

[79] *Agilent 85070E Dielectric Probe Kit 200 MHz to 50 GHz*. Available: http://cp.literature.agilent.com/litweb/pdf/5989-0222EN.pdf

[80] B. Wocher, T. Pfendler, and H. Pfitzemaier, "Method and apparatus utilizing time-expanded pulse sequences for distance measurement in a radar," US Patent 4132991, Jan. 1979.